arXiv:2505.09790v1 [math.OC] 14 May 2025

VALVEFIT: An analysis-suitable B-spline-based surface fitting framework for patient-specific modeling of tricuspid valves

Ajith Moola[a], Ashton M. Corpuz[a], Michael J. Burkhart[b], Colton J. Ross[b], Arshid Mir[c], Harold M. Burkhart[d], Chung-Hao Lee[e], Ming-Chen Hsu[a], Aishwarya Pawar[a,*]

[a]*Department of Mechanical Engineering, Iowa State University, Black Engineering Building, 2529 Union Drive, Ames, Iowa 50011, USA*

[b]*School of Aerospace and Mechanical Engineering, The University of Oklahoma, Felgar Hall, 865 Asp Avenue, Norman, Oklahoma 73019, USA*

[c]*Department of Pediatrics, The University of Oklahoma Health Sciences Center, 1200 N. Children's Ave., Suite 2F, Oklahoma City, Oklahoma 73104, USA*

[d]*Department of Surgery, The University of Oklahoma Health Sciences Center, 800 Stanton L. Young Blvd., Oklahoma City, Oklahoma 73104, USA*

[e]*Department of Bioengineering, University of California, Riverside, 900 University Ave., Riverside, California 92507, USA*

Abstract

Patient-specific computational modeling of the tricuspid valve (TV) is vital for the clinical assessment of heart valve diseases. However, this process is hindered by limitations inherent in the medical image data, such as noise and sparsity, as well as by complex valve dynamics. We present VALVEFIT, a novel GPU-accelerated and differentiable B-spline surface fitting framework that enables rapid reconstruction of smooth, analysis-suitable geometry from point clouds obtained via medical image segmentation. We start with an idealized TV B-spline template surface and optimize its control point positions to fit segmented point clouds via an innovative loss function, balancing shape fidelity and mesh regularization. Novel regularization terms are introduced to ensure that the surface remains smooth, regular, and intersection-free during large deformations. We demonstrate the robustness and validate the accuracy of the framework by first applying it to simulation-derived point clouds that serve as the ground truth. We further show its robustness across different point cloud densities and noise levels. Finally, we demonstrate the performance of

*Corresponding author

Email addresses: arma@iastate.edu (Ajith Moola), amcorpuz@iastate.edu (Ashton M. Corpuz), michael.j.burkhart-1@ou.edu (Michael J. Burkhart), colejr98@gmail.com (Colton J. Ross), arshid-mir@ouhsc.edu (Arshid Mir), harold-burkhart@ouhsc.edu (Harold M. Burkhart), chunghao.lee@ucr.edu (Chung-Hao Lee), jmchsu@iastate.edu (Ming-Chen Hsu), arpawar@iastate.edu (Aishwarya Pawar)

the framework toward fitting point clouds obtained from real patients at different stages of valve motion. An isogeometric biomechanical valve simulation is then performed on the fitted surfaces to show their direct applicability toward analysis. VALVEFIT enables automated patient-specific modeling with minimal manual intervention, paving the way for the future development of direct image-to-analysis platforms for clinical applications.

Keywords: Patient-specific modeling; Surface fitting; Heart valves; Medical imaging; Isogeometric analysis; Periodic B-splines

1. Introduction

Heart valve disease is one of the leading causes of heart failure, resulting in more than 25,000 deaths each year in the United States alone [1–3]. This condition can manifest as *stenosis*, which is the obstruction of blood flow; *regurgitation*, improperly closing valves that result in backflow; or *atresia*, where the valve is underdeveloped and lacks a natural opening for proper blood flow. If left untreated, heart valve disease can severely impair cardiac function; therefore, such medical conditions often require surgical repair or replacement of the valve. One of the severe cases of cardiac disease is congenital heart disease, in which children born with underdeveloped hearts often require several surgeries, further increasing the risk of surgical complications. In particular, patients with hypoplastic left heart syndrome (HLHS) undergo a surgical protocol that involves three successive palliative surgeries: the Norwood procedure, the Glenn procedure, and the Fontan procedure [4–7]. There is an increased risk of tricuspid valve regurgitation (TR) during these surgeries [8–12], which, if not addressed in a timely manner, can cause right ventricle dilation or dysfunction.

In the past decade, advancements in non-invasive cardiac imaging methods have significantly improved the clinical diagnosis and treatment of heart valve diseases [13]. These advanced imaging modalities enable clinicians to generate time-resolved three-dimensional images non-invasively, allowing for preemptive and personalized treatment planning. In cardiac imaging, spatiotemporal echocardiography (4D echo) has emerged as an established non-invasive modality for the visualization of the heart valves, serving as an evaluation of the valve structure and function by providing anatomical and functional information [14]. Despite these advances in non-invasive clinical imaging that enable accurate and earlier prediction of the onset of valve regurgitation and personalized treatment planning [15, 16], technical challenges persist in patient-specific computational modeling of the heart valves [17]. The inherent noise, sparsity, and low resolution of imaging modalities such as echocardiography limit the accurate segmentation and visualization of tricuspid heart valves. Addressing these challenges requires conversion of this low-fidelity imaging data to high-fidelity geometric representations that offer high-resolution surface visualization [18]. The

solution also necessitates the integration of advanced surface fitting methods that can facilitate the automatic generation of patient-specific models, which can be directly used for computational biomechanical analysis [19].

In this paper, we present a novel surface fitting framework that automatically generates patient-specific spline-based surface geometry of the tricuspid valve. The proposed method performs smooth and regular surface deformation of a template surface to fit the 3D point cloud obtained from echocardiographic image segmentation. We validate our framework using tricuspid valve surfaces obtained from simulation data, showing robustness toward different point cloud sampling and noise intensities. We then demonstrate the fitting results using point cloud data from real patients and the application of isogeometric analysis on the fitted surfaces [20]. The rest of the article is organized as follows. In Section 2, we provide an overview of patient-specific computational modeling frameworks for heart valves. The proposed ValveFit framework is introduced in Section 3 and the surface fitting results along with a discussion on the performance are provided in Section 4. We also demonstrate that the surfaces generated by ValveFit are analysis-suitable by performing a simplified valve closure simulation. Finally, we provide concluding remarks and outline future directions in Section 5.

2. Related Work on Patient-Specific Modeling of Heart Valves

The human heart consists of two atrioventricular valves, the tricuspid and mitral valves, and two semilunar valves, the pulmonary and aortic valves [2]. The anatomical complexity of heart valves, which includes asymmetric geometry and thin and flexible leaflet structures, makes accurate patient-specific modeling particularly challenging [21–24]. In addition, during the cardiac cycle, heart valves undergo drastic structural deformation, where the leaflets fold inward as they transition from the open to the closed configuration, further complicating the automatic surface fitting of the fast-moving valves from dynamic time-series images.

Heart valve surface fitting methods play a crucial role in the functional and structural assessment of the valves by providing accurate geometric representations from medical imaging data [25–27]. Several frameworks have been presented in the realm of patient-specific modeling based on surface fitting of point clouds obtained from image segmentation [28, 29]. For example, least squares optimization has been used to fit surfaces to point cloud segmentation data for the tricuspid valves [30]. These methods rely on good-quality image segmentation data to generate analysis-suitable meshes. If the point cloud data from images is sparse, noisy, and incomplete, these existing methods will likely overfit the data, resulting in inaccurate patient-specific valve models that would require considerable manual intervention to fix the models in order to achieve good mesh quality for analysis [31, 32]. Biomechanical models have been used to accurately fit the physiology of the

heart valves [8, 33–35]. However, these methods do not impose stricter geometric regularization constraints to ensure good-quality surfaces during fast valve motion. On the other hand, machine learning-based approaches have been used to model the heart valve geometry directly from medical images, circumventing the image segmentation procedure [36]. However, the accuracy of these methods is dependent on large data from diverse populations, which is typically not available.

B-spline and non-uniform rational B-spline (NURBS) surfaces provide smooth representations of the complex geometry of heart valves. In [37–39], NURBS-based parameterization frameworks were developed to model aortic valves. Isogeometric analysis (IGA) [40–47], which leverages spline-based geometric representations for direct analysis, has been successfully applied to patient-specific structural simulations of aortic valve closure, demonstrating high efficiency compared to traditional finite element (FE) methods [48]. NURBS-based aortic valve models have also been employed in various structural analyses [49–51], fluid-flow simulations [52–54], and fluid–structure interaction studies [55–58], illustrating their versatility and effectiveness in cardiovascular applications. In [59], a deep learning-based framework was proposed for the design and analysis of surgical valves, highlighting the potential of integrating machine learning techniques with geometric modeling approaches. Additionally, in [60, 61], a NURBS-based trileaflet heart valve model was integrated into a neural network finite element (NNFE) framework, enabling rapid simulation of valve closure with a significant speed-up compared to traditional FE solvers. In [20], a generalized modeling and analysis framework for tricuspid valves was introduced, featuring a novel parameterization method for atrioventricular valve modeling. However, the parameterization-based frameworks fall short of capturing the intricate and complex features of the heart valves *automatically* from images and are not generalizable to large patient cohorts. Although surface fitting methods of deforming a template B-spline or NURBS surface to subject-specific point clouds have been proposed [62–66], these approaches are not robust to complex changes in the valve surface across a large patient database or for mapping dynamic surfaces at different time points of valve motion during the cardiac cycle. Under large deformation, these methods can produce warped or intersected surfaces that would need manual changes to the mesh to make it analysis-suitable [67].

Existing surface fitting approaches face several challenges that limit their clinical utility. Current approaches risk overfitting to noisy and sparse point cloud data and therefore rely on high-quality image segmentation, which is difficult to achieve with real echocardiographic images. Many surface fitting approaches lack proper geometric regularization constraints during deformation, especially during large valve motion, resulting in twisting of surface geometry, which is not analysis-suitable. These approaches require manual interventions to correct unsatisfactory meshes for analysis. To address these limitations, we propose the VALVEFIT framework, where we address the

challenges of generalizable heart valve fitting by using a smooth B-spline surface fitting differentiable framework with novel regularization constraints. The VALVEFIT framework enables the automatic generation of complex valve geometry. In the present study, we also demonstrate the effectiveness of the framework for large-scale, patient-specific modeling, addressing the challenges with respect to inter-patient anatomical variability. Finally, we will also demonstrate the robustness of our method to generate smooth and analysis-suitable patient-specific valve surfaces considering various levels of Gaussian noise in point cloud data. The key features of VALVEFIT can be summarized as follows:

- A GPU accelerated B-spline surface fitting framework using automatic differentiation, enabling faster B-spline surface evaluations and gradient computation.
- Novel geometric regularization loss terms that ensure mesh regularity and prevent mesh distortion even during large deformation, while still accurately fitting the point clouds.
- Ensuring robustness toward noise, point cloud densities, and anatomical variability between patients.
- Automatic generation of patient-specific, analysis-suitable valve geometries without the need for manual interventions.

These innovations enable the VALVEFIT framework to reliably generate analysis-suitable valve geometries directly from noisy and sparse clinical data with minimal manual intervention, laying the foundation for the future development of direct image-to-analysis platforms for clinical applications.

3. Methods

In this section, we provide a detailed description of the proposed valve fitting framework, VALVEFIT. We first describe the image acquisition process and the segmentation of the tricuspid valve geometry from imaging data in Section 3.1. We then describe the proposed surface fitting framework for the automatic generation of patient-specific valve geometries in Section 3.2.

3.1. Image Acquisition and Segmentation

This study is performed using echocardiographic imaging data from the University of Oklahoma Health Sciences Center of retrospectively enrolled HLHS-afflicted patients before the Stage I (Norwood) palliation surgery (IRB approval #14112). In brief, routine 4-dimensional (4D, i.e., X, Y, Z, time) full-volume echocardiographic data is collected for multiple cardiac cycles using a Philips EPIQ ultrasound machine (Philips, NV) equipped with a 5 MHz transthoracic matrix-array transducer. Patient echo imaging data are obtained through ECG-gated acquisitions over 6 to 8 con-

secutive heartbeats to ensure reproducible and reliable data [68]. The echocardiogram images are converted into a Cartesian Digital Imaging and Communications in Medicine (3D DICOM) format in QLAB Cardiac Analysis software (Philips, NV).

Segmentations of the tricuspid valve are performed using 3D Slicer [69, 70] at time instants between end-diastole (ED) and end-systole (ES) within the same cardiac cycle. First, the annulus is segmented by rotating the coronal image plane around the annulus in 10-degree increments and manually placing a point at the leaflet hinge point of each angular increment, which is identified by analyzing sequential time points in the echocardiogram sequence, to generate a point cloud consisting of 36 points (Fig. 1(a)). Then, points are added to manually trace the leaflets using the sagittal and coronal image frames with an approximate point density of 6.2 mm (Fig. 1(b)).

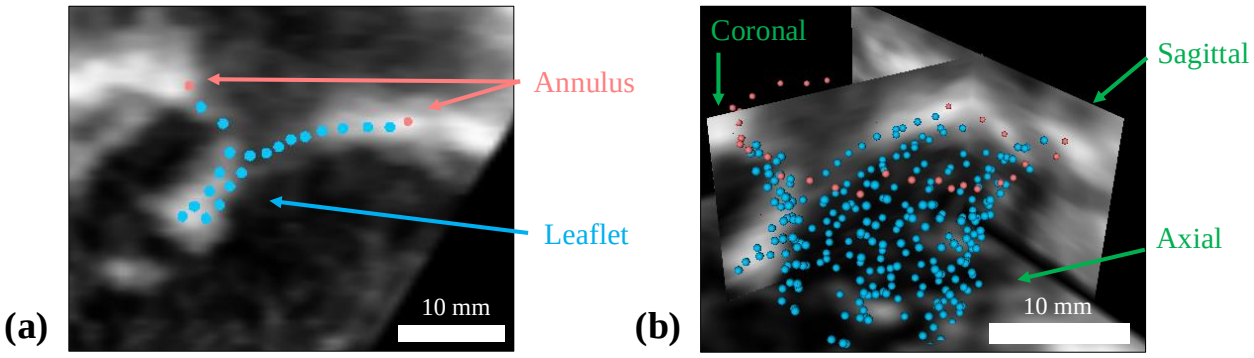


Figure 1: Representative echocardiogram imaging data of a newborn with hypoplastic left heart syndrome (HLHS) and the segmented point cloud for the tricuspid valve (TV) apparatus: **(a)** coronal view and **(b)** 3D perspectives. Segmented points (red) for the TV annulus and segmented points (blue) for the three TV leaflets.

After the valves are segmented, the X, Y, and Z coordinates of each leaflet are imported to MATLAB (MathWorks, USA), where an in-house program is used to classify each coordinate as belonging to the septal (SL), anterior (AL), or posterior leaflet (PL). Briefly, the X and Y coordinates of the commissure locations (i.e., the region between each leaflet), as manually identified using 3D Slicer, are first converted to polar coordinates (r, θ), with the septal-anterior commissure used as the reference angle (i.e., $\theta_{(SL-AL)} = 0^{\circ}$). Using the values of θ at each commissure location, intervals are constructed for each leaflet for categorization of the leaflet segmentation data points. For example, a point i was classified as belonging to the anterior leaflet if $\theta_{(SL-AL)} < \theta_i < \theta_{(AL-PL)}$.

3.2. THE VALVEFIT *Framework*

The proposed VALVEFIT framework generates an accurate and smooth surface representation of the tricuspid heart valve using B-splines. This is achieved by deforming a template B-spline surface to fit unstructured point clouds derived from the image segmentation of 4D echocardiographic data. The surface is deformed by moving control points based on the minimization of a loss

function using gradient-descent optimization. The template geometry is constructed as a single patch B-spline surface, informed by the anatomical structure of the tricuspid valve, in order to ensure topological similarity. The anterior, posterior, and septal leaflets of the tricuspid heart valve (shown in Fig. 2(a)) are attached to a fibrous ring known as the annulus. These leaflets are anchored to the papillary muscles of the right ventricle through chordae tendineae, which prevent the leaflets from inverting during ventricular contraction [2, 26].

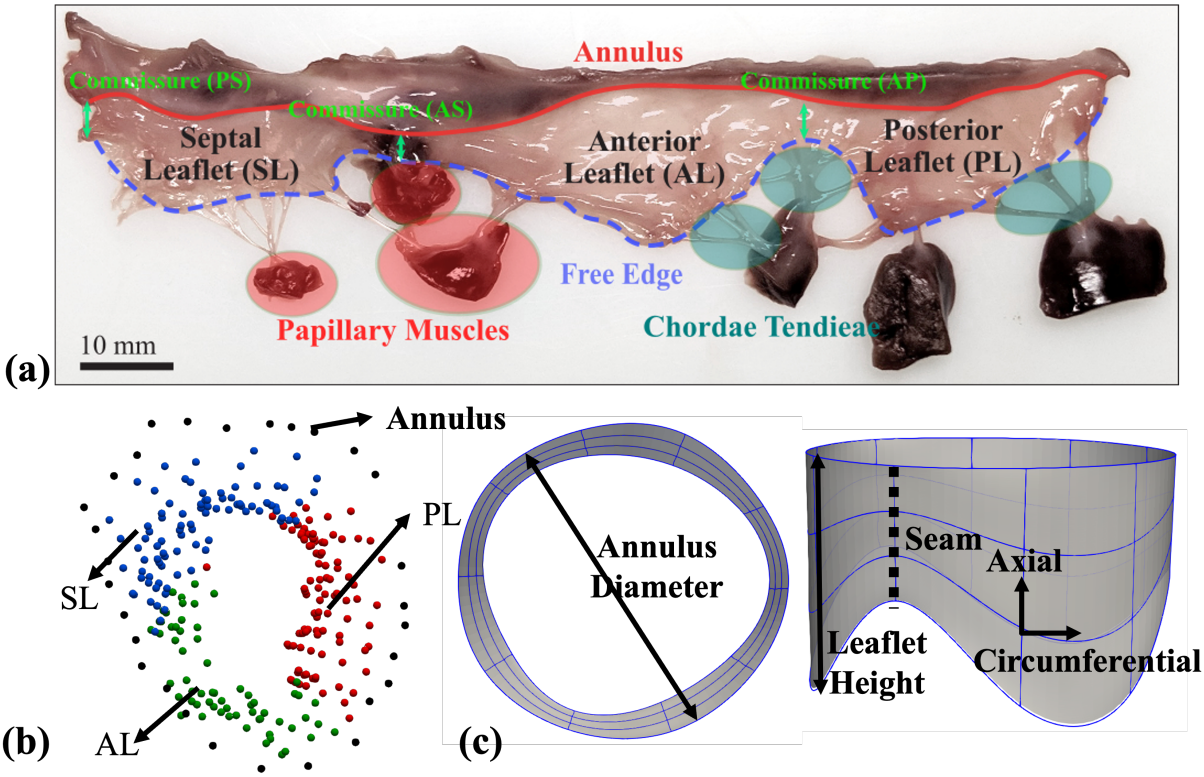


Figure 2: **(a)** Excised porcine tricuspid valve (TV) showing the three leaflets—septal (SL), anterior (AL), and posterior (PL)—along with their commissures. **(b)** Point cloud representation of a patient's TV annulus (black) and the three leaflets: SL (blue), AL (green), and PL (red). **(c)** Template geometry constructed using a single-patch periodic B-spline surface, shown in both top and side views. Idealized template geometry is generated with the annulus modeled as a circular ring and the leaflets with equal heights. Surface parameterization is carried out using knot vectors: $\mathcal{U} := \{0, 0, 0, 0.33, 0.66, 1, 1, 1\}$ along the axial direction and $\mathcal{V} := \{-0.3, -0.2, -0.1, 0, 0.1, 0.2, 0.3, 0.4, 0.5, 0.6, 0.7, 0.8, 0.9, 1, 1.1, 1.2, 1.3\}$ along the circumferential direction.

3.2.1. The Template Geometry

Due to its annular ring and leaflet configuration, the tricuspid valve topology is similar to that of a cylinder. In the template geometry, the annulus is modeled as a circular ring, and the leaflets are assigned equal heights to represent an idealized tricuspid valve in the open configuration during diastole (see Fig. 2(c)) [20, 27]. Note that a cylindrical surface could be directly used as the

template geometry due to its topological similarity to the tricuspid valve. However, we chose an idealized template TV surface to better capture the key anatomical features of the target point clouds shown in Fig. 2(b), including the three-leaflet topology and the characteristic annular shape.

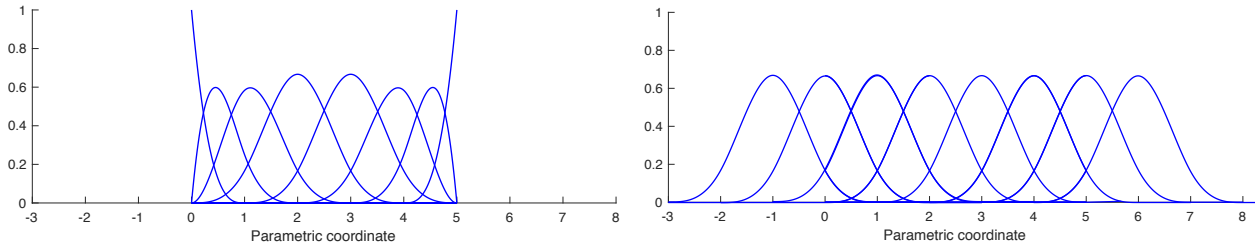
To enable higher continuity across the seam (Fig. 2(c)), the template geometry is constructed as a single patch B-spline surface using periodic B-splines. This B-spline surface undergoes non-linear deformation through loss function minimization, resulting in a patient-specific TV B-spline surface at the end of the fitting process. A B-spline surface ($\mathbf{S} \in \mathbb{R}^3$) can be described as

$$\mathbf{S}(u,v) = \sum_{i=1}^{n} \sum_{j=1}^{m} B_{i,p}(u) B_{j,q}(v) \mathbf{P}_{i,j}\,, \tag{1}$$

where $B_{i,p}(u)$ and $B_{j,q}(v)$ are univariate B-spline basis functions of degrees p and q, defined on the knot vectors $\mathcal{U} := \{u_1, u_2, \ldots, u_{n+p+1}\}$ and $\mathcal{V} := \{v_1, v_2, \ldots, v_{m+q+1}\}$, corresponding to the u- (circumferential) and v- (axial) parametric directions, respectively [71]. The surface point is given by $\mathbf{S}(u,v) = (x(u,v),\ y(u,v),\ z(u,v))$, where $x(u,v)$, $y(u,v)$, and $z(u,v)$ represent the Cartesian coordinates of the point. Here, n and m denote the number of basis functions in each parametric direction, and $\mathbf{P}_{i,j} \in \mathbb{R}^3$ are the control points. The template geometry is constructed as a periodic B-spline surface with periodicity enforced along the circumferential direction. Accordingly, $B_{i,p}(u)$ is defined as an *open non-periodic* B-spline using *clamped* knot vectors, while $B_{j,q}(v)$ is a *closed periodic* B-spline defined over *unclamped* knot vectors. To create a closed B-spline curve, which can be either periodic or non-periodic, the control points at the two ends of the curve must be closed or overlapped. The distinction between a closed non-periodic and a closed periodic B-spline curve, along with their respective constructions, is shown in Figs. 3 and 4. In Fig. 3(a), cubic B-spline basis functions are defined over the *clamped* knot vector: $\{0,0,0,0,1,2,3,4,5,5,5,5\}$. As seen in Fig. 4(a), overlapping the first and last control points results in a closed B-spline curve. However, the continuity at the parametric boundary is reduced to C^0 due to knot multiplicity at the ends of the knot vector. In Fig. 3(b), cubic basis functions are defined over the *unclamped* knot vector: $\{-3,-2,-1,0,1,2,3,4,5,6,7,8\}$. By wrapping three control points at the two ends of the curve, we can achieve C^2 continuity in the interior as well as across the parametric boundary, as seen in Fig. 4(b) [71].

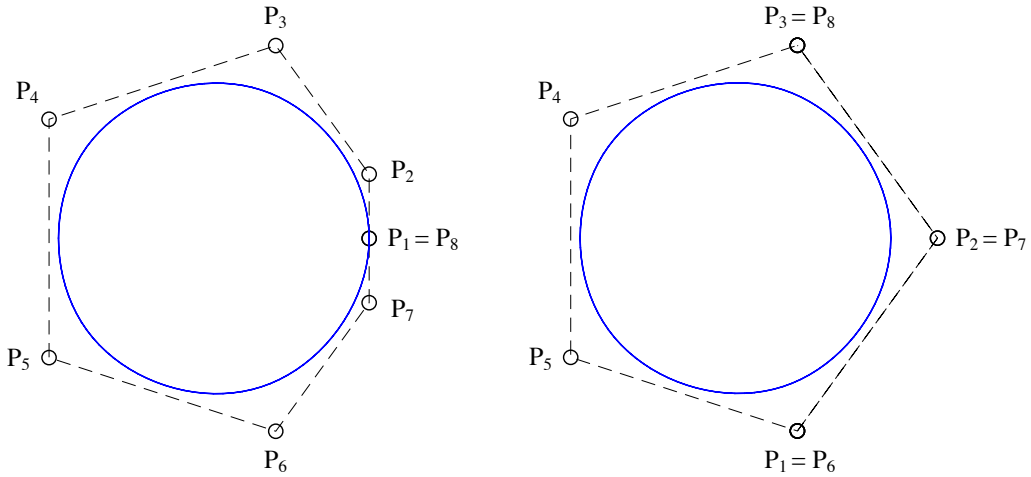
3.2.2. The Loss Function

The proposed VALVEFIT framework performs iterative deformation through the minimization of a loss function using gradient descent optimization. To ensure the generation of an analysis-suitable, patient-specific TV geometry [72, 73], we enforce smooth and regular deformation of the template surface at each iteration. We define the loss function ($\mathcal{L}$), consisting of a shape fidelity term and a



(a) **(b)**

Figure 3: Comparison of cubic B-spline basis functions for **(a)** clamped and **(b)** unclamped knot vectors, defined as $\{0, 0, 0, 0, 1, 2, 3, 4, 5, 5, 5, 5\}$ and $\{-3, -2, -1, 0, 1, 2, 3, 4, 5, 6, 7, 8\}$, respectively.



(a) **(b)**

Figure 4: Comparison of **(a)** closed non-periodic and **(b)** closed periodic cubic B-spline curves. The periodic curve in **(b)** achieves C^2 continuity across the parametric boundary, whereas the non-periodic curve in **(a)** maintains only C^0 continuity.

mesh regularization term, as

$$\mathcal{L}(\mathbf{S}, \mathbf{Q}) = \mathcal{E}_{\text{fid}}(\mathbf{S}, \mathbf{Q}) + \mathcal{E}_{\text{reg}}(\mathbf{S}) \,, \tag{2}$$

where $\mathbf{S}$ denotes the template B-spline surface and $\mathbf{Q}$ denotes the target point cloud. The shape fidelity term $\mathcal{E}_{\text{fid}}(\mathbf{S}, \mathbf{Q})$ ensures that the fitted surface closely approximates the target point cloud. It is defined as

$$\mathcal{E}_{\text{fid}}(\mathbf{S}, \mathbf{Q}) = w_{\text{cd}}\, d_{\text{CD}}(\mathbf{S}, \mathbf{Q}) + w_{\text{hd}}\, d_{\text{HD}}(\mathbf{S}, \mathbf{Q}) + w_{\text{a}}\, d_{\text{CD}}(\mathbf{A}_{\text{S}}, \mathbf{A}_{\text{Q}}) \,, \tag{3}$$

where $d_{\text{CD}}(\mathbf{S}, \mathbf{Q})$ denotes the one-sided Chamfer distance. $d_{\text{CD}}(\mathbf{S}, \mathbf{Q})$ evaluates the average squared distance between every point in the point cloud and the closest point on the template surface. The Hausdorff distance, $d_{\text{HD}}(\mathbf{S}, \mathbf{Q})$, measures the maximum distance between the template

surface and the point cloud. $d_{\text{CD}}(\mathbf{A}_{\text{S}}, \mathbf{A}_{\text{Q}})$ calculates the Chamfer distance between the parametric boundary on the template surface closest to the annulus $\mathbf{A}_{\text{S}} := \mathbf{S}(u = u_0)$ and the points corresponding to the annulus in the target point cloud $\mathbf{A}_{\text{Q}}$. w_{cd}, w_{hd}, and w_{a} are the weights controlling the relative contributions of each distance term within the shape fidelity term.

In Eq. (3), $d_{\text{CD}}(\mathbf{S}, \mathbf{Q})$, $d_{\text{HD}}(\mathbf{S}, \mathbf{Q})$ and $d_{\text{CD}}(\mathbf{A}_{\text{S}}, \mathbf{A}_{\text{Q}})$ are computed using a distance matrix, $\mathbf{D} \in \mathbb{R}^{N \times M}$, which encodes pairwise distances between the points sampled on the template surface and those in the target point cloud. Let $\mathbf{s}_k = \mathbf{S}(u_k, v_k)$, for $k = 1, ..., M$, denote points sampled from the template surface $\mathbf{S}$, and let $\mathbf{q}_l \in \mathbf{Q}$, for $l = 1, ..., N$, denote points in the target point cloud $\mathbf{Q}$. Each element D_{kl} of the distance matrix is defined as

$$D_{kl} = ||\mathbf{s}_k - \mathbf{q}_l||, \quad \forall\, \mathbf{s}_k \in \mathbf{S}\,,\ \mathbf{q}_l \in \mathbf{Q}\,. \tag{4}$$

For each surface point $\mathbf{s}_k \in \mathbf{S}$, the nearest neighbor distance to the target point cloud $\mathbf{Q}$ is given by $m_k^S = \min_l D_{kl}$. Similarly, for each point $\mathbf{q}_l \in \mathbf{Q}$, the nearest neighbor distance to $\mathbf{S}$ is $m_l^Q = \min_k D_{kl}$. We define the one-sided Chamfer distance $d_{\text{CD}}(\mathbf{S}, \mathbf{Q})$ using only distances from the point cloud to the B-spline surface. This prevents multiple points on the template surface from mapping to a single point in the target point cloud. We thus define $d_{\text{CD}}(\mathbf{S}, \mathbf{Q})$ as

$$d_{\text{CD}}(\mathbf{S}, \mathbf{Q}) = \frac{1}{N} \sum_{l=1}^{N} m_l^Q. \tag{5}$$

Next, the Hausdorff distance is defined as

$$d_{\text{HD}}(\mathbf{S}, \mathbf{Q}) = \max\{\max_k\, m_k^S\,;\, \max_l\, m_l^Q\}. \tag{6}$$

The Hausdorff distance term ensures that the largest deviations between the surface and the point cloud are minimized, hence addressing outliers in the point cloud, particularly at the boundaries. Finally, the computation of $d_{\text{CD}}(\mathbf{A}_S, \mathbf{A}_Q)$ follows an approach similar to that used for computing d_{CD}. However, it computes the two-sided Chamfer distance, which also includes the mean of the nearest neighbor distances from $\mathbf{A}_S$ to $\mathbf{A}_Q$. The sensitivity to outliers and noise can be modulated by adjusting the weights w_{cd}, w_{hd}, and w_{a} in Eq. (3).

The regularization term $\mathcal{E}_{\text{reg}}(\mathbf{S})$ imposes smoothness and regularity constraints on the surface to obtain a smooth parameterization in the physical domain and prevent element distortions or self-intersections. It comprises two terms:

$$\mathcal{E}_{\text{reg}}(\mathbf{S}) = w_{\text{orth}}\, R_{\text{orth}}(\mathbf{S}) + w_{\text{norm}}\, R_{\text{norm}}(\mathbf{S}). \tag{7}$$

The weights w_{orth} and w_{norm} allow us to control the influence of each of the above two terms in Eq. (7), allowing for adjustments based on specific mesh quality requirements. We can efficiently compute the tangent vectors and normal vectors required for Eq. 7 by using the automatic differentiation capabilities of JAX [74]. We evaluate the partial derivatives of the surface coordinates (x, y, and z) with respect to the parametric coordinates u and v by evaluating the Jacobian matrix, J, using automatic differentiation as

$$J = \begin{bmatrix} \frac{\partial x}{\partial u} & \frac{\partial y}{\partial u} & \frac{\partial z}{\partial u} \\ \frac{\partial x}{\partial v} & \frac{\partial y}{\partial v} & \frac{\partial z}{\partial v} \end{bmatrix}^T . \tag{8}$$

The tangent vectors, $\mathbf{T}_u$ and $\mathbf{T}_v$, and the surface unit normal vector, $\mathbf{N}$, are computed from the Jacobian matrix as follows:

$$\mathbf{T}_u(u,v) = \frac{\partial \mathbf{S}}{\partial u} = \begin{bmatrix} \frac{\partial x}{\partial u} & \frac{\partial y}{\partial u} & \frac{\partial z}{\partial u} \end{bmatrix}^T , \tag{9}$$

$$\mathbf{T}_v(u,v) = \frac{\partial \mathbf{S}}{\partial v} = \begin{bmatrix} \frac{\partial x}{\partial v} & \frac{\partial y}{\partial v} & \frac{\partial z}{\partial v} \end{bmatrix}^T , \tag{10}$$

$$\mathbf{N}(u,v) = \frac{\mathbf{T}_u(u,v) \times \mathbf{T}_v(u,v)}{\|\mathbf{T}_u(u,v) \times \mathbf{T}_v(u,v)\|}. \tag{11}$$

To improve the local orthogonality between the u and v parametric directions in the physical domain and reduce excessive folding of the surface, we define the orthogonality regularization term, $R_{\text{orth}}(\mathbf{S})$, as

$$R_{\text{orth}}(\mathbf{S}) = \frac{1}{M} \sum_{k=1}^{M} \left\| \frac{\mathbf{t}_k^u \cdot \mathbf{t}_k^v}{\|\mathbf{t}_k^u\| \, \|\mathbf{t}_k^v\|} \right\| , \tag{12}$$

where $\mathbf{t}_k^u = \mathbf{T}_u(u_k, v_k)$ and $\mathbf{t}_k^v = \mathbf{T}_v(u_k, v_k)$ denote the tangent vectors evaluated at each sampled parametric point (u_k, v_k), and M is the number of sampled points in the parametric domain. By calculating the cosine of the angle between the tangent vectors, R_{orth} avoids excessive skewing or twisting of surface elements during deformation. By controlling the variation of the vertical (z) component of the unit normal vector $\mathbf{N}(u,v)$, the second term in Eq. 7, $R_{\text{norm}}(\mathbf{S})$, penalizes self-intersections of the template surface and is defined as

$$R_{\text{norm}}(\mathbf{S}) = \max_{1 \le k \le M} \|\mathbf{n}_k^z - \bar{\mathbf{n}}^z\| , \tag{13}$$

where $\mathbf{n}_k^z$ denotes the z-component of the unit normal vector $\mathbf{N}(u,v)$ evaluated at the parametric coordinate (u_k, v_k), and $\bar{\mathbf{n}}^z$ is the mean value of the z-component of the normal vector over all the sampled parametric points. In order to prevent abrupt changes in surface orientation and intersec-

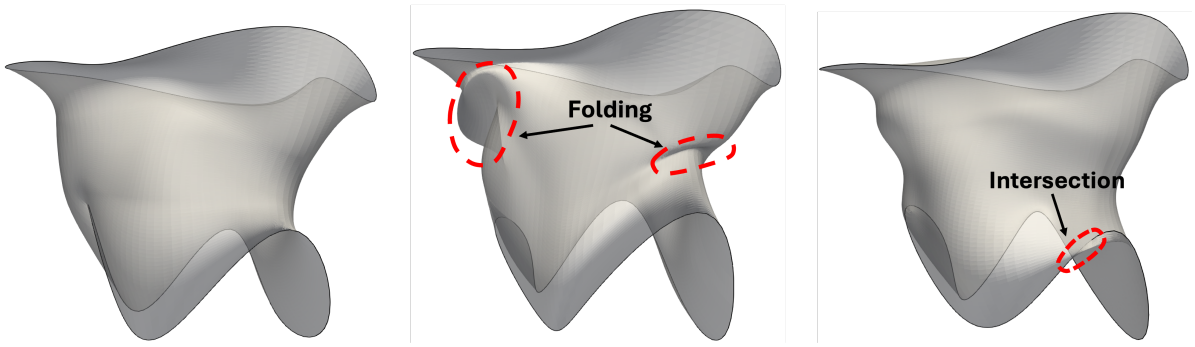


Figure 5: B-spline surfaces fitted: **(a)** with both R_{orth} and R_{norm} included in the loss function, resulting in a smooth surface free from severe folding or self-intersections; **(b)** without R_{orth}, leading to severe folding due to loss of orthogonality of parametric lines; and **(c)** without R_{norm}, resulting in visible self-intersections due to large variations in surface normal orientation.

tions in the fitted surfaces, this term penalizes significant deviations in surface normal orientation along the (z) direction. Fig. 5 illustrates how the regularization terms in $\mathcal{E}_{\text{reg}}$ affect surface fitting results. In Fig. 5(b) the surface is fitted without the orthogonality term R_{orth}, resulting in severe folding of the surface— although no self-intersections occur. In contrast, fitting the surface without R_{norm} leads to self-intersections, as seen in Fig. 5(c). When both R_{orth} and R_{norm} are included in the loss function, the resulting surface is free from severe folding and self-intersections (as shown in Fig. 5(a)).

3.2.3. Surface Fitting

To accurately fit the template B-spline surface to target point clouds obtained from image segmentation, we use differentiable programming [64, 65] during surface fitting. In the template B-spline surface (Eq. (1)), the parametric coordinates u and v are fixed during optimization, and the control point positions $\mathbf{P}$ are optimized to minimize the loss function. The gradient of the loss function with respect to $\mathbf{P}$ is given as

$$\nabla_{\mathbf{P}}\mathcal{L} = \frac{\partial \mathcal{L}}{\partial \mathbf{S}} \frac{\partial \mathbf{S}}{\partial \mathbf{P}}. \tag{14}$$

The partial derivative of the surface with respect to each control point $\mathbf{P}_{i,j}$ is given by

$$\frac{\partial \mathbf{S}}{\partial \mathbf{P}_{i,j}} = B_{i,p}(u) B_{j,q}(v). \tag{15}$$

During loss minimization, calculating the gradients of the loss function (Eq. (2)) with respect to the surface $\mathbf{S}$ is more complex than computing the derivatives in Eq. (15). For example, the gradient

of the Chamfer distance term is given as

$$\frac{\partial d_{\text{CD}}}{\partial \mathbf{S}} = \frac{\partial}{\partial \mathbf{S}} \left(\frac{1}{N} \sum_{l=1}^{N} \min_{k} \|\mathbf{s}_k - \mathbf{q}_l\| \right), \tag{16}$$

where $\mathbf{s}_k$ are points sampled from the B-spline surface and $\mathbf{q}_l$ are points from the target point cloud. Manual gradient evaluation is laborious and ineffective since it would be necessary to derive and implement the gradients for each term in the loss function, which would involve significant bookkeeping and be prone to error. This complexity emphasizes how crucial it is to use automatic differentiation in our surface fitting framework in order to compute gradients effectively and precisely. The optimization of control points $\mathbf{P}$ to minimize the loss function is performed using the Adam optimizer [75]. The gradient of the loss function with respect to all control points is given by

$$\nabla_{\mathbf{P}} \mathcal{L} = \left[\frac{\partial \mathcal{L}}{\partial \mathbf{P}_{1,1}}, \frac{\partial \mathcal{L}}{\partial \mathbf{P}_{1,2}}, \ldots, \frac{\partial \mathcal{L}}{\partial \mathbf{P}_{n,m}} \right]^T, \tag{17}$$

and each control point is updated iteratively as

$$\mathbf{P}_{i,j}^{(t+1)} = \mathbf{P}_{i,j}^{(t)} - \delta \frac{\partial \mathcal{L}}{\partial \mathbf{P}_{i,j}^{(t)}}, \tag{18}$$

where δ is the learning rate and t denotes the time step. The template B-spline surface $\mathbf{S}_0$ is initialized with predefined knot vectors and polynomial degrees at the start of the optimization process. The target point clouds, representing valve configurations across the cardiac cycle, are sequentially ordered from the open to the closed state, or vice versa. To ensure consistency in scale, position, and orientation, the template surface is first globally aligned to the corresponding target point clouds using affine transformations. In order to accurately fit $\mathbf{S}_0$ to $\mathbf{Q}_1$, non-linear deformation of the template surface is carried out by minimization of the loss function (Eq. (2)). The resulting fitted surface, $\mathbf{S}_1$, serves as the updated template surface for fitting the next point cloud in the sequence, $\mathbf{Q}_2$. This process allows for consistent surface fitting results throughout the cardiac cycle and is carried out throughout the entire sequence. The detailed algorithm is outlined in Algorithm 1.

4. Results

In this section, we demonstrate the performance of the VALVEFIT framework in accurately fitting B-spline surfaces to point cloud data. A validation study employing synthetic point clouds generated from structural simulations of heart valve motion is presented in Section 4.1. Since these

Algorithm 1 VALVEFIT: Patient-Specific Surface Fitting for Tricuspid Valve Geometry

Input: Template geometry with predefined parametrization: basis functions $(\mathbf{B}_u, \mathbf{B}_v)$ and control points $\mathbf{P}_0$; sequence of target point clouds $\{\mathbf{Q}_1, \mathbf{Q}_2, \ldots, \mathbf{Q}_n\}$; maximum number of iterations t_{max}; learning rate δ; weights $\{w_{\text{cd}}, w_{\text{hd}}, w_{\text{a}}, w_{\text{orth}}, w_{\text{norm}}\}$

Output: Control points of fitted surfaces $\{\mathbf{P}_1, \mathbf{P}_2, \ldots, \mathbf{P}_n\}$

for $r = 1$ to n **do**
  Set: $\mathbf{P}_r \leftarrow \mathbf{P}_{r-1}$ // Use previous fit as new template
  Apply affine transformation to align surface $\mathbf{S}_r$ to point cloud $\mathbf{Q}_r$: update $\mathbf{P}_r$
  for $t = 1$ to t_{max} **do**
    Compute surface points: $\mathbf{S}_r^{(t)} \leftarrow \mathbf{B}_u \otimes \mathbf{B}_v \cdot \mathbf{P}_r^{(t)}$
    Evaluate loss: $\mathcal{L}(\mathbf{S}_r^{(t)}, \mathbf{Q}_r)$ with weights $\{w_{\text{cd}}, w_{\text{hd}}, w_{\text{a}}, w_{\text{orth}}, w_{\text{norm}}\}$ // Eq. (2)
    Compute the gradient of the loss function with respect to control points: $\nabla \mathbf{P}_r^{(t)} \leftarrow \frac{\partial \mathcal{L}}{\partial \mathbf{P}_r^{(t)}}$
    Update control points: $\mathbf{P}_r^{(t+1)} \leftarrow \mathbf{P}_r^{(t)} - \delta \cdot \nabla \mathbf{P}_r^{(t)}$
  end for
  Save final control points: $\mathbf{P}_r \leftarrow \mathbf{P}_r^{(t_{\text{max}})}$
end for

point clouds are uniform and noise-free, they are used as the ground truth for TV geometry. Using these point clouds, we further investigate the effect of point cloud density (Section 4.2) and noise (Section 4.3) on fitting accuracy. Finally, in Section 4.4, we apply the framework towards echocardiographic data acquired at multiple stages in the cardiac cycle to demonstrate its utility in generating patient-specific valve geometries.

To quantitatively evaluate the surface fitting accuracy, we introduce a dimensionless error metric, the scaled Nearest Neighbor Distance (sNND). While the Nearest Neighbor Distance (NND) measures the minimum distance from each point in the point cloud to the fitted surface, it is scale-dependent, varying with the size of the geometry. To address this limitation, sNND normalizes this nearest neighbor distance by the square root of the surface area, allowing for consistent comparison across valve geometries of different anatomical sizes in patients. For each point $\mathbf{q}_l$ in the target point cloud, where $l = 1, \cdots, N$, the sNND to the fitted surface $\mathbf{S}$ of area $\mathcal{A}(\mathbf{S})$ is defined as

$$\text{sNND}(\mathbf{q}_l, \mathbf{S}) = \frac{\min_k \|\mathbf{q}_l - \mathbf{s}_k\|}{\sqrt{\mathcal{A}(\mathbf{S})}} \,. \tag{19}$$

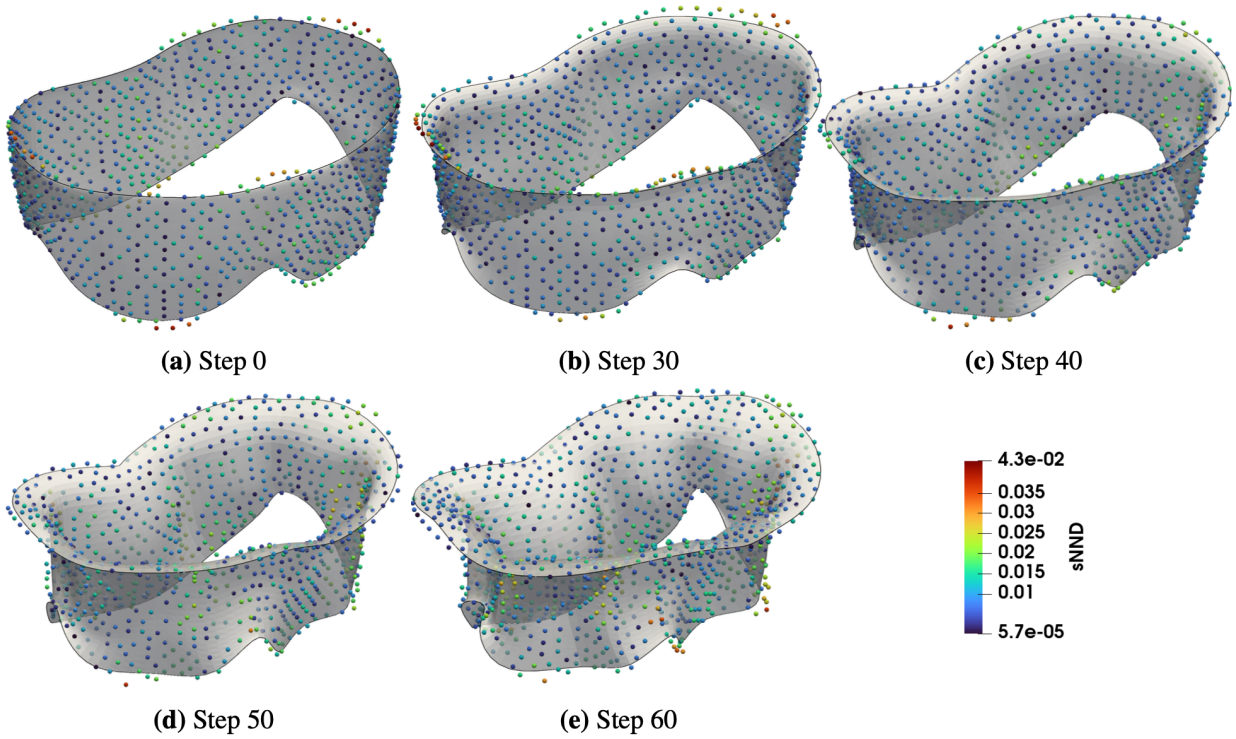
4.1. Validation Study with Simulation Data

Point clouds obtained from image segmentation of echocardiogram images are often sparse, noisy, partial, and may not accurately represent the tricuspid valve surface. Ascertaining the accuracy of the fitted geometry using error metrics such as sNND, with respect to noisy point clouds, is not a reliable measure of the robustness of the fit, as the target point cloud itself may not accurately

represent the underlying geometry. A very low sNND error for extremely noisy point clouds may in fact indicate that the fitted surface is overfitting the noise, resulting in an inaccurate representation of the underlying geometry. The resulting geometry is generally less smooth, of poor quality, and thus requires considerable manual effort to make it analysis-suitable. Therefore, we first validate our surface fitting algorithm by fitting B-spline surfaces to point clouds sampled from benchmark B-spline surfaces obtained from structural simulations of heart valve motion.

These structural simulations are carried out using an IGA-based tricuspid valve parameterization framework [20]. This framework defines the annulus during the systolic phase of the cardiac cycle and determines the commissure and leaflet locations along the annular curve. These locations are then used to define the valve heights, whose endpoints are interpolated to construct the free-edge curve of the leaflet. From the annular and free-edge curves, a Gordon surface [71] is generated to reconstruct the leaflets' surface parameterization. For the chordae tendineae, we define the positions of the papillary muscles in R^3 space, by specifying the number and spacing of the chordae. A steady-state structural simulation is performed on a dense analysis mesh by applying a follower pressure load normal to the leaflet surface, continuing until valve closure. Further details on the surface parameterization and simulation methodology can be found in [20]. The resulting simulation-derived point clouds represent idealized yet exact, noise-free surfaces, where accurate fitting results at different stages of valve motion are expected. To match the point cloud density typically observed in image segmentations of patient data, we sample approximately 1500 points from the simulation surface for fitting. This ensures that the benchmark point cloud data has a similar point cloud density as the patient data.

The template geometry shown in Fig. 2 is first re-parameterized using uniform knot vectors, resulting in 23 control points with degree $p = 3$ along the u direction and 5 control points with degree $q = 2$ along the v direction. The template surface is then aligned to the target point cloud at simulation step 0 (Fig. 6(a))using affine transformations. The positions of the control points are then updated by surface fitting, where each fitted B-spline surface acts as a template for the next point cloud in the sequence. The weight parameters in the loss function (Eq. (2)) were set to $w_{\text{cd}} = 20$, $w_{\text{hd}} = 0.5$, $w_{\text{a}} = 0$, $w_{\text{orth}} = 10$, and $w_{\text{norm}} = 5$. These weights are constant during the sequential fitting of the B-spline surface. The weight w_{a} is set to zero because the point cloud for the validation study is not further segmented into annulus and leaflet regions. Therefore, this dataset does not have explicit labels for the points belonging to the annulus and leaflets. In Fig. 6, we show the fitted B-spline surfaces overlaid with the corresponding point cloud data at each simulation step. The sNND error is computed for each point in the point cloud to evaluate local fitting accuracy. Based on the results, we can see that the resulting surfaces are smooth, intersection-free, and closely aligned with the point clouds across all the stages of valve motion. Complex fold-



(a) Step 0 **(b)** Step 30 **(c)** Step 40

(d) Step 50 **(e)** Step 60

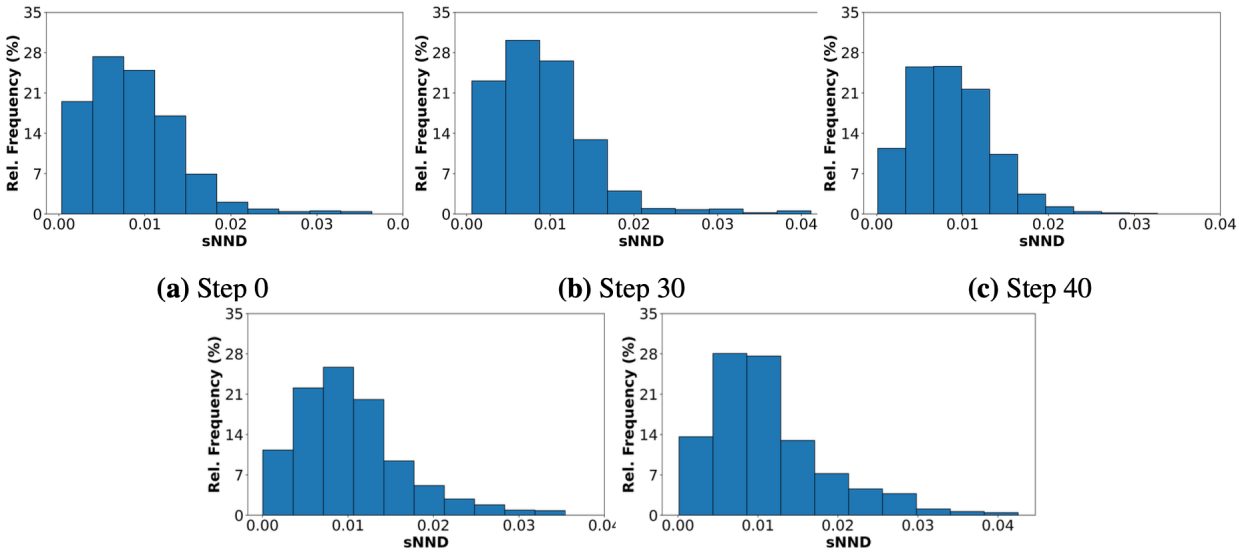
Figure 6: The fitted B-spline surfaces are shown overlaid with the corresponding benchmark point clouds, obtained at multiple steps during the structural simulation of valve motion: **(a)** Step 0, **(b)** Step 30, **(c)** Step 40, **(d)** Step 50, and **(e)** Step 60. The point clouds are colored based on the sNND error with respect to the fitted surface.

ing structures of the geometry are effectively captured, while maintaining smoothness and surface regularity.

Table 1: Minimum, maximum, and mean sNND errors between the fitted surface and the target point clouds at different simulation steps.

Step	Minimum sNND	Maximum sNND	Mean sNND
0	3.06×10^{-4}	0.0363	0.0087
30	2.23×10^{-4}	0.0430	0.0091
40	5.66×10^{-5}	0.0353	0.0087
50	1.07×10^{-4}	0.0343	0.0103
60	6.38×10^{-5}	0.0342	0.0109

The histograms shown in Fig. 7 show consistent sNND error distributions across all the simulation steps, with the majority of points concentrated in the low sNND range (below 0.02). Table 1 presents a quantitative assessment of the surface fitting accuracy using the sNND error metric, where lower values indicate better alignment between fitted surfaces and point cloud data. Here, we report the minimum, mean, and maximum sNND errors for each fitting result. The mean sNND error quantifies the overall fitting accuracy, while the difference between maximum and



(a) Step 0 **(b)** Step 30 **(c)** Step 40

(d) Step 50 **(e)** Step 60

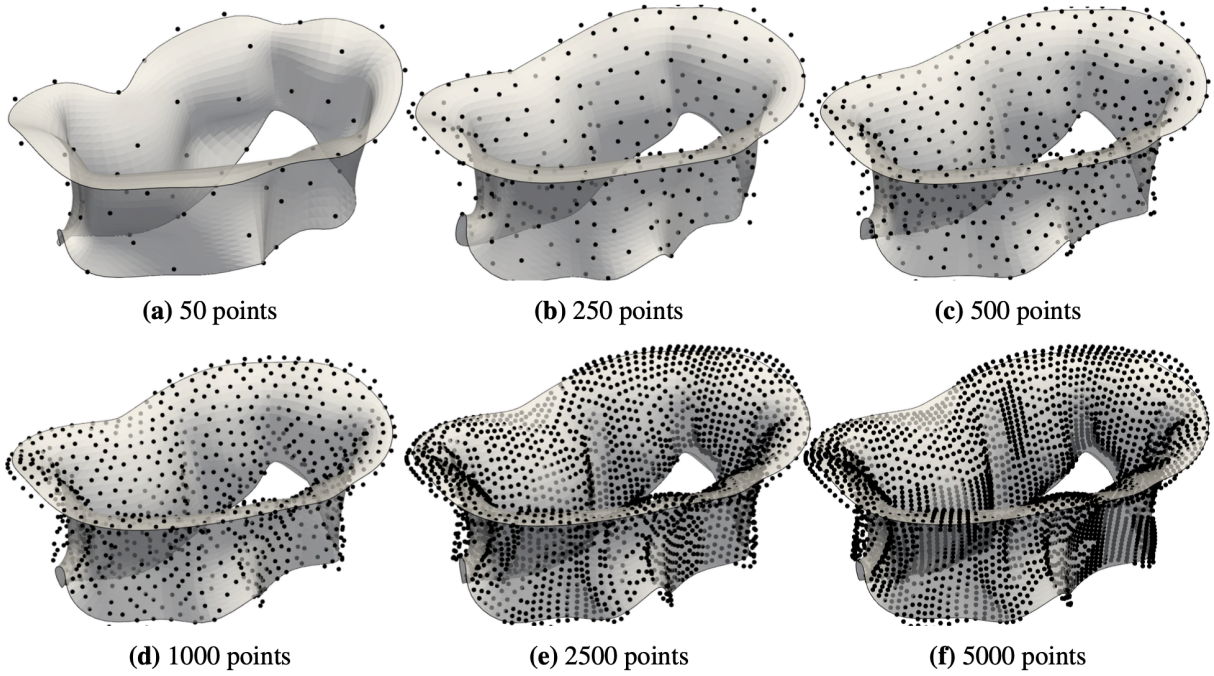
Figure 7: Histograms showing the percentage of points with respect to sNND error at different simulation steps for the validation study. The distributions are consistent across all steps, with the majority of points exhibiting low fitting error, concentrated in the range below 0.02. This indicates the stable performance of the VALVEFIT framework over time.

minimum sNND errors quantifies the amount of variability in the fitting accuracy. Across all the simulation steps, low sNND error values are observed, with minimum sNND values ranging between 5.66×10^{-5} and 3.06×10^{-4}. In all the simulation steps, the maximum sNND values stay below 0.0430. The mean sNND values range between 0.0087 and 0.0109, showing consistent fitting at all stages of valve motion. We can see that high accuracy is maintained across most of the geometry, with maximum sNND values localized to regions of greater complexity, particularly near leaflet edges and areas undergoing folding. The framework effectively balances geometric accuracy with the requirement of maintaining intersection-free surfaces throughout the cardiac cycle.

4.2. Surface fitting sensitivity with respect to point cloud sampling

We further evaluate the sensitivity of the VALVEFIT framework to point cloud sampling density by fitting valve surfaces to point clouds of increasing densities. For this study, we performed surface fitting on the point cloud corresponding to the simulation step 60 of valve motion. The fitted B-spline surfaces are overlaid with the sampled point clouds, as shown in Fig. 8. For each point cloud density, Table 2 reports the minimum, maximum, and mean sNND error values between the fitted surfaces and their corresponding point clouds.

Based on the results shown in Table 2 and Fig. 8, we observe that the sNND error continuously



(a) 50 points **(b)** 250 points **(c)** 500 points

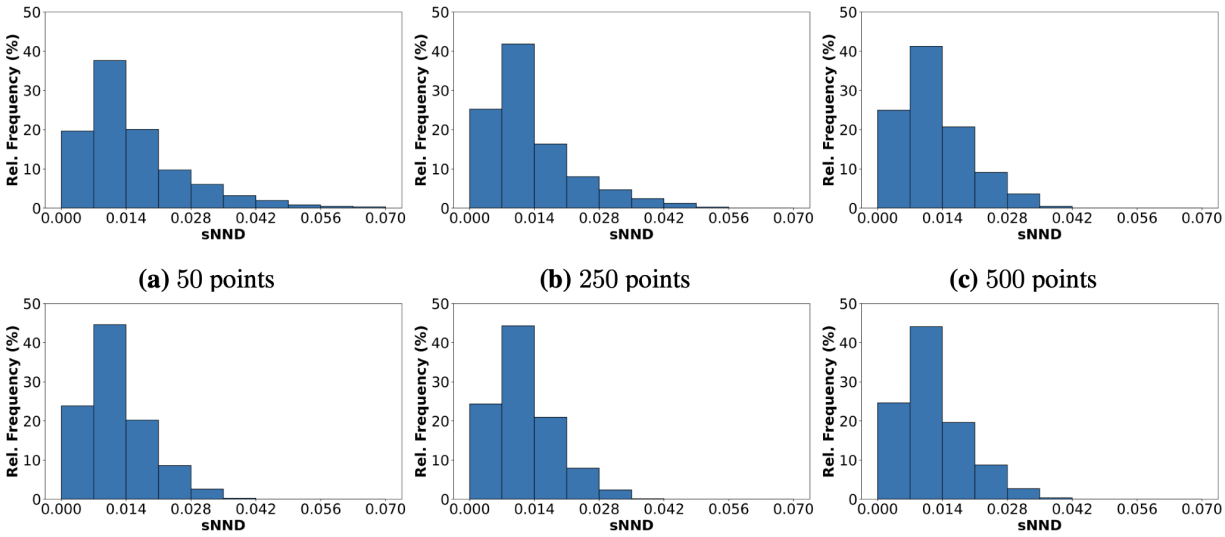
(d) 1000 points **(e)** 2500 points **(f)** 5000 points

Figure 8: Fitted B-spline surfaces overlaid with target point clouds obtained at simulation step 60 (see Fig. 6(e)), sampled at varying densities (**(a)**–**(f)**: 500 to 5000 points). Higher point cloud densities provide more detailed geometric information, enabling more accurate fitting results.

decreases from 0.0155 to 0.0121 as the point cloud density increases from 50 to 5000. This is because, in order to capture the intricate details of the valve geometry during fitting, a higher point cloud density is required to provide a more detailed geometric representation. However, we observe that the mean sNND error does not decrease further beyond a point cloud density of 2500 points. This is because the fitted B-spline surface is evaluated at 2500 points for the calculation of the sNND metric. When calculating the Chamfer distance—which involves nearest neighbor distances from the point cloud to the surface points and vice versa—the resolution of the surface sampling becomes the limiting factor. Further improvements in the sNND metric due to an increase in sampling have no noticeable impact on nearest neighbor distance values once the point cloud density becomes greater than the number of points sampled on the B-spline surface. The percentage of points in the lower error bracket increases with point cloud density, as can be seen in Fig. 9 and Table 2. As point cloud density increases, the difference between the maximum and minimum sNND errors also decreases. This is because a higher point cloud density reduces the chance of overfitting by incorporating more point cloud-to-surface distance evaluations into the Chamfer distance.

Table 2: Minimum, maximum, and mean sNND errors between the fitted B-spline surface and target point clouds at varying densities.

Point Count	Minimum sNND	Maximum sNND	Mean sNND
50	5.06×10^{-5}	0.0718	0.0155
250	5.70×10^{-5}	0.0528	0.0132
500	8.03×10^{-5}	0.0396	0.0124
1000	1.40×10^{-4}	0.0382	0.0121
2500	8.85×10^{-5}	0.0364	0.0119
5000	4.02×10^{-4}	0.0374	0.0121



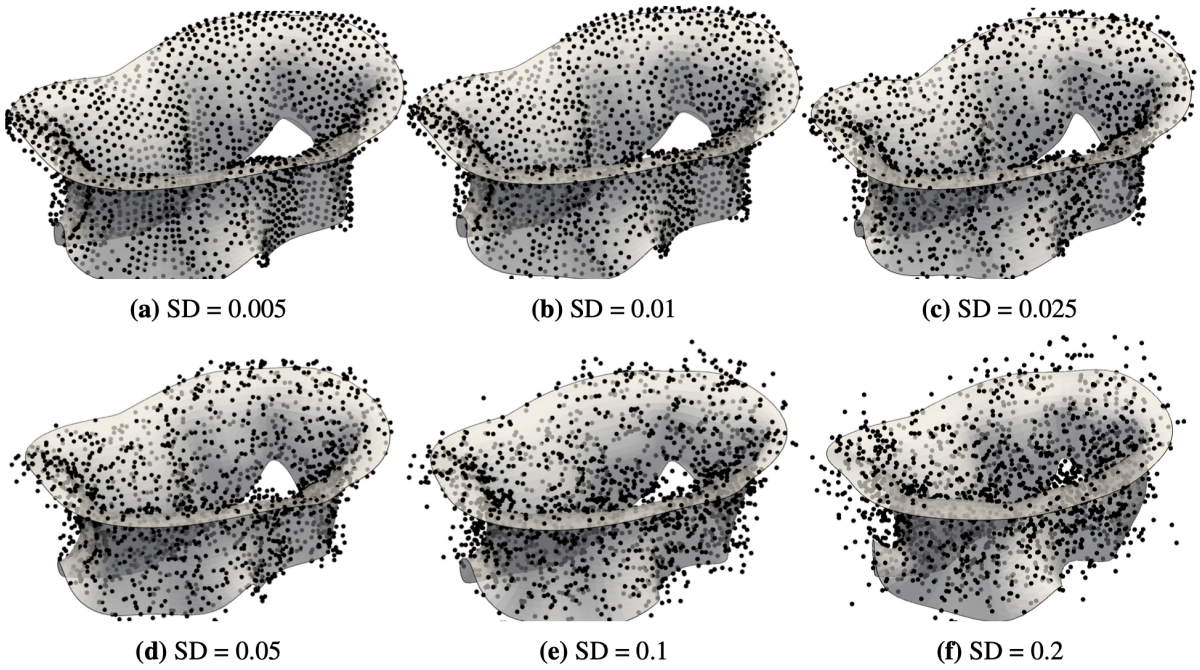
(a) 50 points **(b)** 250 points **(c)** 500 points

(d) 1000 points **(e)** 2500 points **(f)** 5000 points

Figure 9: Histograms showing the percentage of points with respect to sNND error at different point cloud densities for simulation data.

4.3. Fitting sensitivity with respect to noise

In Fig. 10, we evaluate the robustness of the VALVEFIT framework under varying levels of noise in the point cloud data. Here, random perturbations were added to the point cloud consisting of 2500 points at simulation step 60. The goal was to simulate the noise typically observed in point cloud data derived from echocardiographic images (Section 3.1). Gaussian noise was added with increasing standard deviations (SD) of $0.005, 0.01, 0.025, 0.05, 0.1,$ and 0.2 [76], representing a specific degree of perturbation. For each noise level, we report the point-wise fitting error using the sNND error metric, which quantifies the deviations of the fitted surface from the ground truth surface, defined by the original noise-free point cloud. Despite increasing noise, the VALVEFIT framework successfully captures the finer features of the surface while at the same time generating smooth and intersection-free surfaces. Even while the noise levels increase, the fitted surfaces maintain a close approximation of the underlying geometry without overfitting. The mean and



(a) SD = 0.005 **(b)** SD = 0.01 **(c)** SD = 0.025

(d) SD = 0.05 **(e)** SD = 0.1 **(f)** SD = 0.2

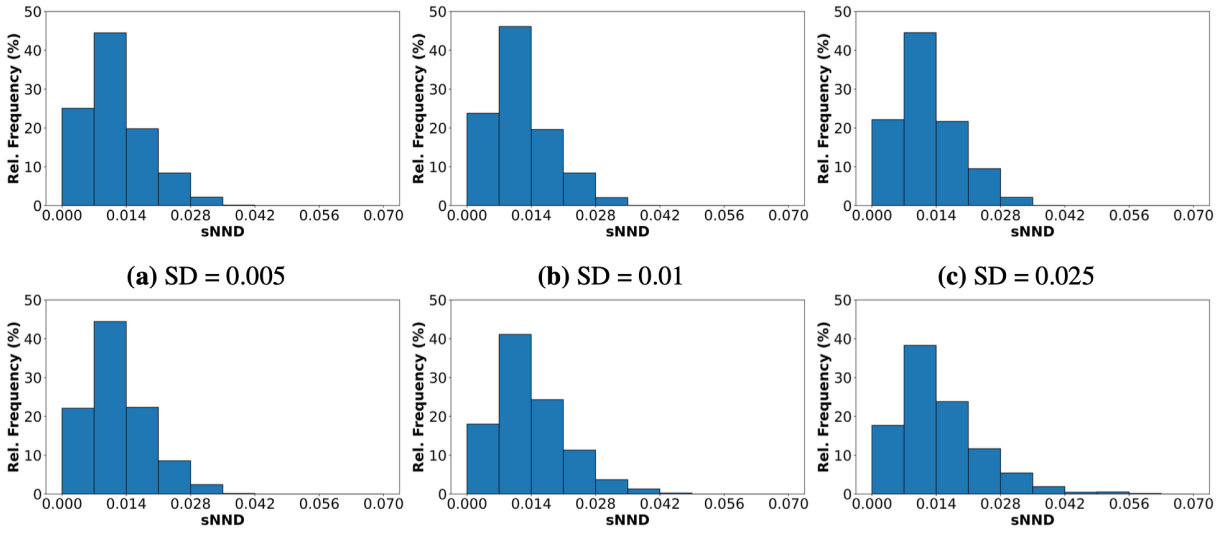
Figure 10: Fitted B-spline surfaces overlaid with target noisy point clouds obtained at simulation step 60, Gaussian noise at increasing standard deviations is added: **(a)**–**(f)** correspond to SD values of 0.005, 0.01, 0.02, 0.05, and 0.2, respectively. Despite increasing noise levels, fitted B-spline surfaces are smooth, accurate, and intersection-free.

Table 3: Minimum, maximum, and mean sNND errors between the fitted B-spline surface and target point clouds with added Gaussian noise at increasing standard deviations.

SD	Minimum sNND	Maximum sNND	Mean sNND
0	6.71×10^{-4}	0.0363	0.0118
0.005	4.17×10^{-4}	0.0359	0.0118
0.01	6.96×10^{-4}	0.0352	0.0119
0.025	7.63×10^{-4}	0.0359	0.0122
0.05	9.61×10^{-4}	0.0376	0.0122
0.1	7.58×10^{-4}	0.0464	0.0138
0.2	9.25×10^{-4}	0.0590	0.0146

maximum sNND values gradually increase as the noise levels rise from 0.036 to 0.042, according to the sNND errors in Table 3. In Fig. 11, we similarly observe few points falling into high error bins as the noise levels rise. However, the sNND error does not significantly increase, showcasing minimal distortion of the B-spline surfaces due to noise.

In Sections 4.1–4.3, we demonstrate the capability of the ValveFit framework to accurately fit point cloud data under different stages of valve motion, point cloud densities and Gaussian noise levels. When fitting point cloud data sequentially, the framework consistently maintains mean



(a) SD = 0.005 **(b)** SD = 0.01 **(c)** SD = 0.025

(d) SD = 0.05 **(e)** SD = 0.1 **(f)** SD = 0.2

Figure 11: Histogram showing the percentage of points with respect to sNND error at different point cloud noise levels (SD from 0.005 to 0.2) for simulation data. We observe that while the spread of errors slightly increases with increasing noise levels, the majority of the points lie in the lower error range, showing the robustness of VALVEFIT framework towards noise.

sNND error values between 0.0342 and 0.0430, even during complex valve motion. Table 2 shows that the VALVEFIT framework obtained a mean sNND value of 0.0155 even with a relatively sparse point cloud density of only 50 points, which is comparable to the mean sNND values obtained at higher point cloud densities. As can be observed in Table 3, we also report a slight increase in sNND values as the amount of Gaussian noise in the point cloud increases. This validation study shows that the VALVEFIT framework exhibits fitting robustness under a range of conditions by accurately reconstructing surfaces that closely match the ground truth geometry across a range of noise levels and point cloud densities.

4.4. Surface Fitting for Patient Data

In this section, we perform surface fitting using VALVEFIT framework on echocardiographic imaging data obtained from two patients. The point cloud data is labeled based on relative time, normalized with the duration of one cardiac cycle (T). In this normalized scale, $0.0\,T$ is defined as the beginning of the cardiac cycle, corresponding to the time of minimum right ventricular pressure. $1.0\,T$ represents the end of the same cardiac cycle and corresponds to the beginning of the next cardiac cycle ($1.0\,T_i = 0.0\,T_{i+1}$). Important physiological events are also marked within a cardiac cycle, where $0.3\,T$ corresponds to end-diastole (ED), when the valve leaflets are coapted, and approximately at $0.45\,T$, which corresponds to end-isovolumetric contraction [77]. Figs. 12 and 13 show surface fitting results for the first patient data at $0.0\,T$, $0.05\,T$, $0.12\,T$, $0.17\,T$, $0.22\,T$,

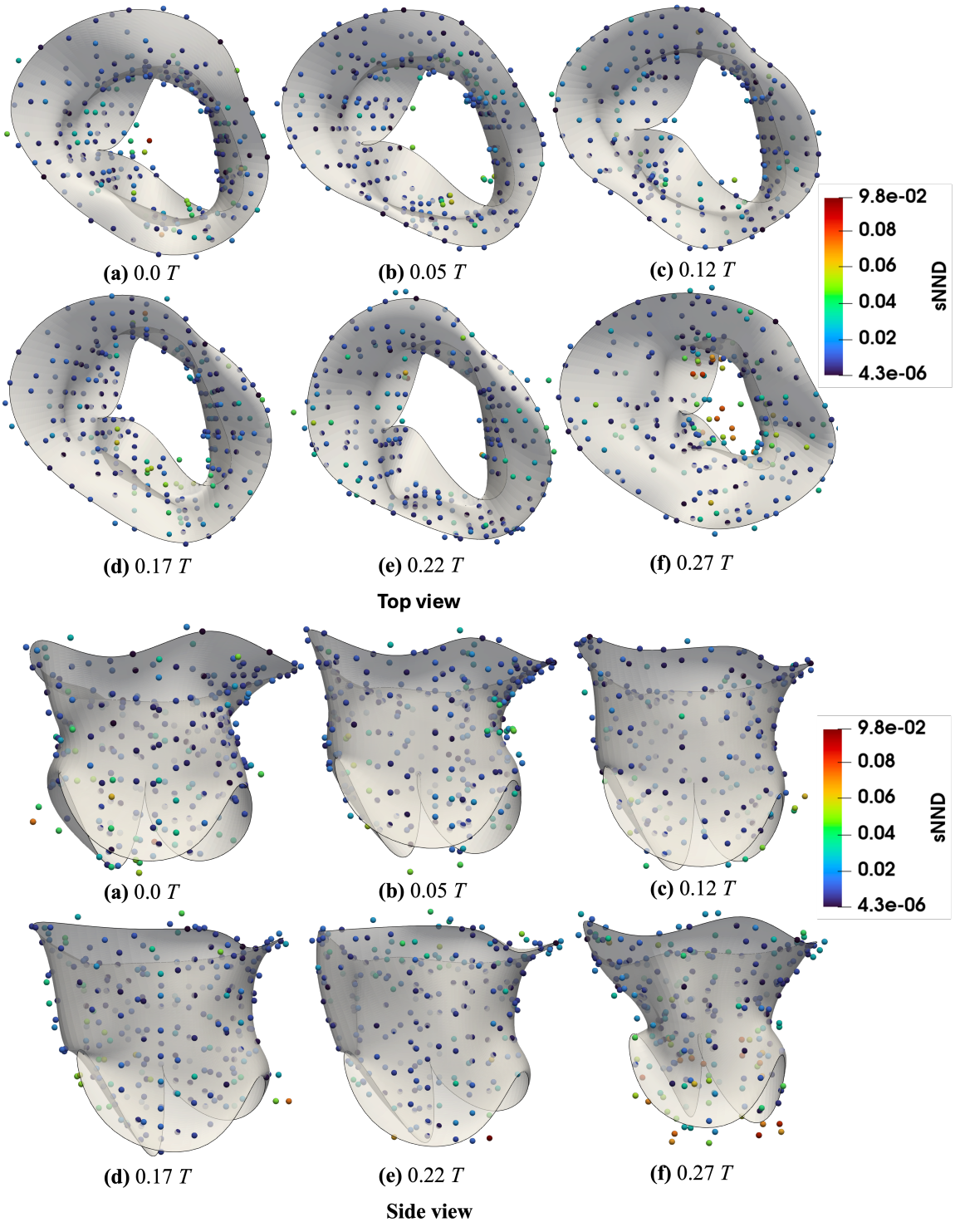
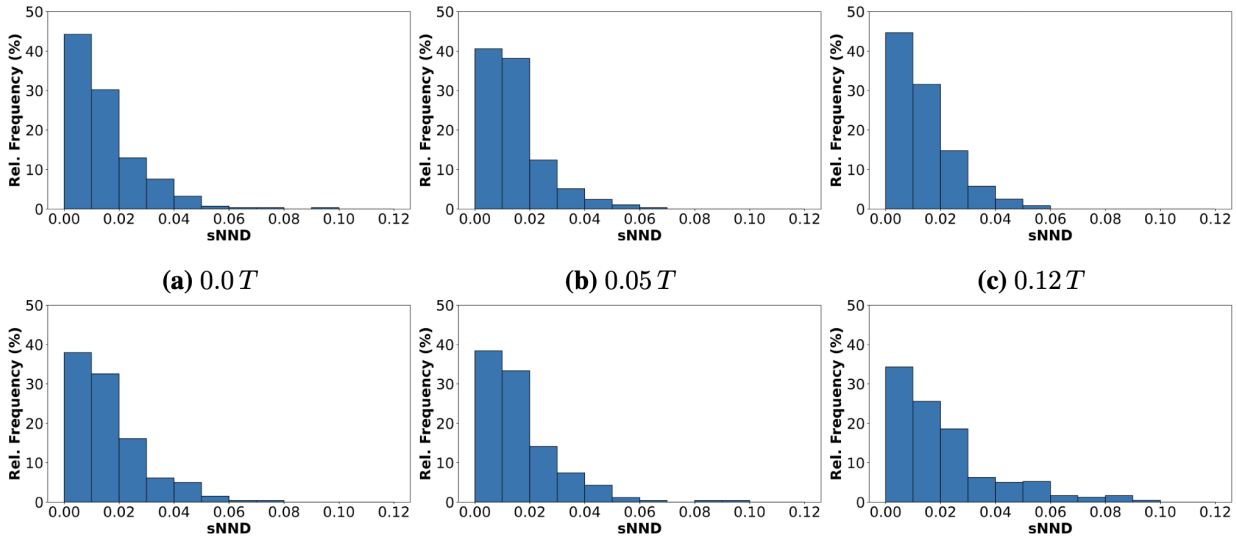


Figure 12: Patient 1 dataset: Fitted surfaces overlaid with the target point clouds at six stages of the cardiac cycle: **(a)** At the beginning of cardiac cycle $0.0\,T$, **(b)** $0.05\,T$, **(c)** $0.12\,T$, **(d)**$0.17\,T$, **(e)** $0.22\,T$, and **(f)** near the end-diastole $0.27\,T$. The first two rows show the top view of the fitted surfaces, while the bottom two rows show the side view of the fitted surfaces. Each point in the target point cloud is colored according to its sNND error.

and $0.27\,T$), while Figs. 14 and 15 show the results for the second patient data at $0.75\,T$, $0.80\,T$, $0.85\,T$, $0.93\,T$, and $1.00\,T$).



(a) $0.0\,T$ **(b)** $0.05\,T$ **(c)** $0.12\,T$

(d) $0.17\,T$ **(e)** $0.22\,T$ **(f)** $0.27\,T$

Figure 13: Patient 1 dataset: Percentage of points in the dataset plotted against the sNND error at different time points across the cardiac cycle. Each subplot corresponds to fitting accuracy at a certain time point in the cardiac cycle.

The template geometry shown in Fig. 2, is used for fitting patient data. The template surface parameterization consists of 13 control points with degree $p = 3$ basis functions along the u direction and 5 control points with degree $q = 2$ basis functions along the v direction. The weight parameters in Eq. (3) for the first patient data were set to $w_{\text{cd}} = 20$, $w_{\text{hd}} = 0.5$, $w_{\text{a}} = 1$, $w_{\text{orth}} = 10$, and $w_{\text{norm}} = 5$. These weights are identical to the weights used for the validation study in Section 4.1, except that for fitting patient data we are using $w_{\text{a}} = 1$ instead of zero. This is because we have access to point clouds where the annulus and leaflets have been separately segmented. For the second patient data, we observed higher noise intensity in the point clouds. To avoid overfitting the noise, we thus increased the relative importance of the regularization terms in the loss function (Eq. (2)) compared to the shape fidelity terms. Specifically, we decreased the weights w_{cd} from 20 to 5 and w_{a} from 1 to 0.1, ensuring that the surface does not try to overfit the noisy point cloud and remains smooth.

In Figs. 13 and 15, we show histograms of the sNND error distributions from the target point clouds to the fitted surface for Patients 1 and 2, respectively. For the Patient 1 dataset (Fig. 13), the maximum observed sNND error is 0.0982, with the majority of points reporting sNND errors below 0.04. The maximum observed sNND error for the Patient 2 dataset (Fig. 15) is 0.1359, with a greater percentage of points reporting an sNND error below 0.06. The distributions show consistent

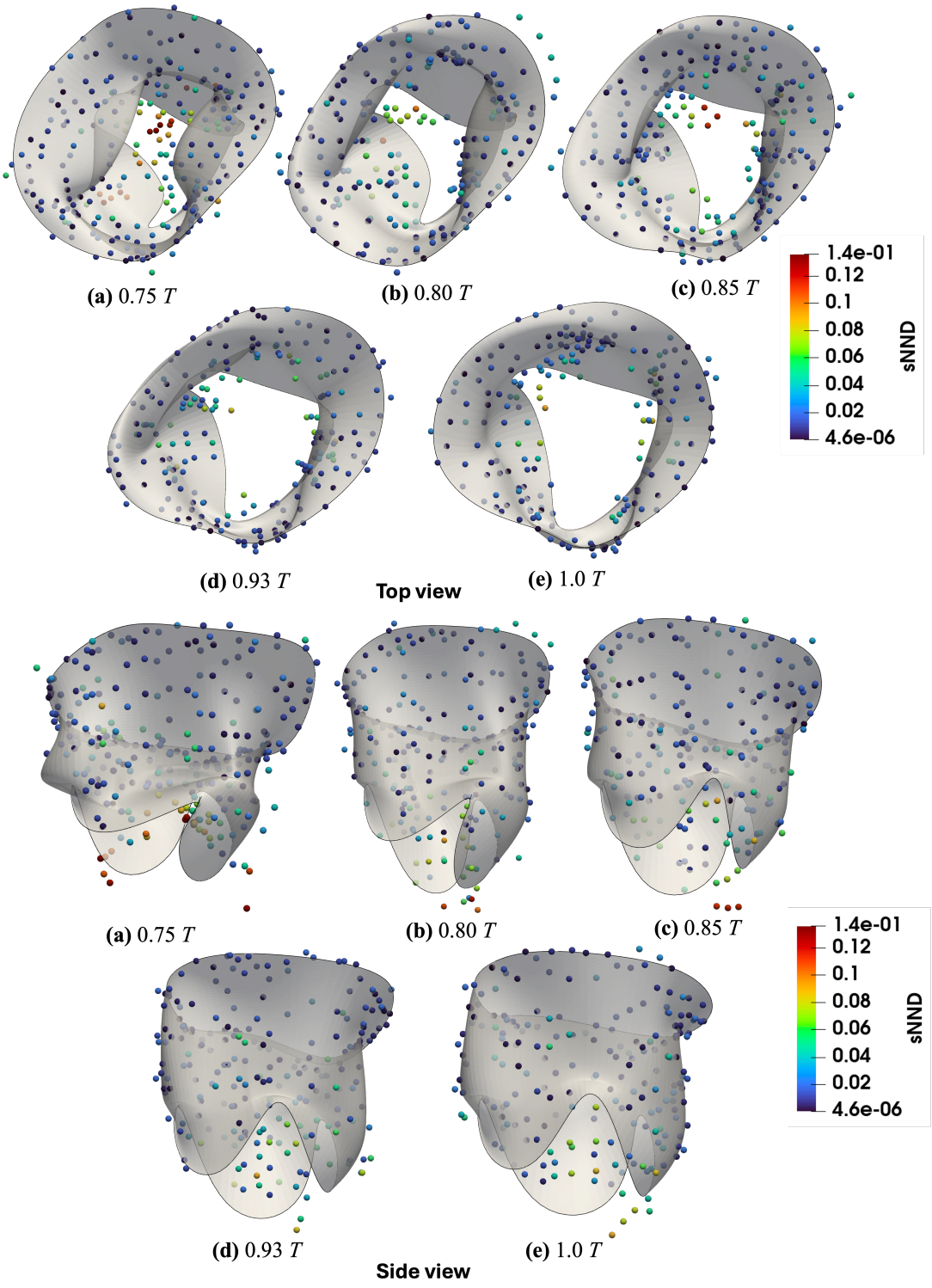
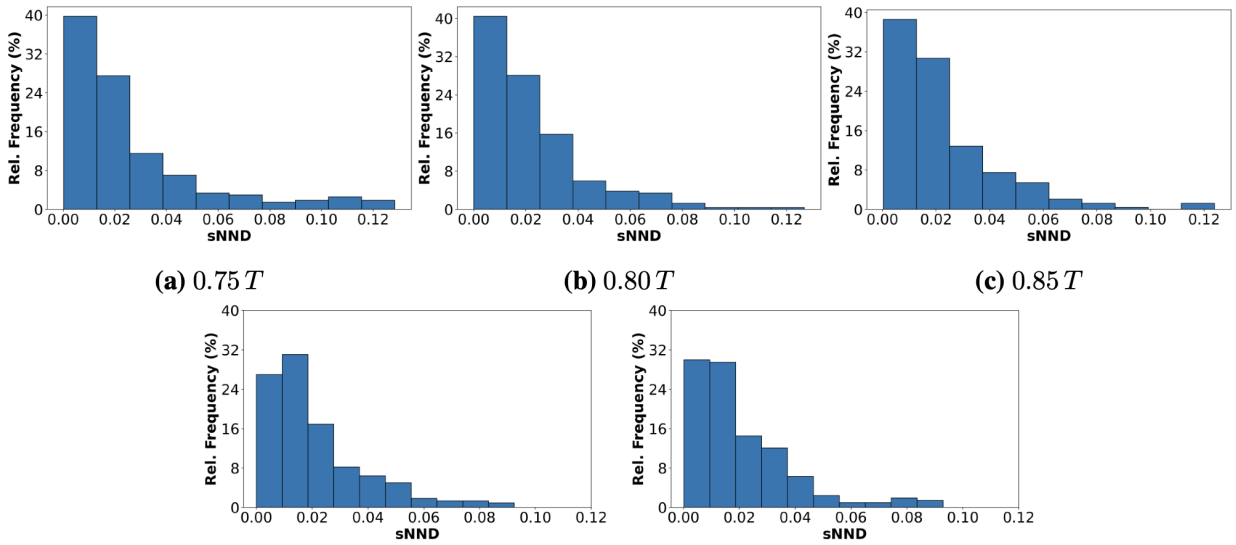


Figure 14: Patient 2 dataset: Fitted TV B-spline surfaces overlaid with the corresponding target point clouds captured at 5 stages of the cardiac cycle: **(a)** $0.75\,T$, **(b)** $0.80\,T$, **(c)** $0.85\,T$, **(d)** $0.93\,T$, and **(e)** at the end of the cardiac cycle $(1.00\,T)$. The top two rows show the top view of the surfaces, while the bottom two rows show the side view. Each point in the target point cloud is colored according to its sNND error, providing a visual representation of the accuracy of the fitted surface at that location.



(a) $0.75\,T$ **(b)** $0.80\,T$ **(c)** $0.85\,T$

(d) $0.93\,T$ **(e)** $1.0\,T$

Figure 15: Patient 2 dataset: Percentage of points in the dataset plotted against the sNND error at different time points across the cardiac cycle. Each subplot corresponds to fitting accuracy at a certain time point in the cardiac cycle

Table 4: Patient 1 dataset: Minimum, maximum and mean sNND errors between the fitted B-spline surface and target point clouds at different stages of the cardiac cycle.

Step	Minimum sNND	Maximum sNND	Mean sNND
$0.0\,T$	9.35×10^{-6}	0.0904	0.0152
$0.05\,T$	4.35×10^{-6}	0.0599	0.0142
$0.12\,T$	5.47×10^{-6}	0.0629	0.0143
$0.17\,T$	1.84×10^{-5}	0.0744	0.0155
$0.22\,T$	7.82×10^{-6}	0.0982	0.0152
$0.27\,T$	5.33×10^{-6}	0.0896	0.0225

performance of the framework throughout the cardiac cycle. According to Table 4, the mean sNND errors for the Patient 1 dataset are between 0.0142 and 0.0225 across the six stages, showing the framework's consistently stable performance throughout the cardiac cycle. The maximum sNND values ranged from 0.0599 to 0.0982, with slightly higher values at $0.22\,T$ and $0.27\,T$. These values were found to correlate with increased geometric complexity at the closed valve configurations.

Compared to the Patient 1 dataset, the sNND errors for the Patient 2 dataset (Table 5) were higher, with mean sNND values ranging from 0.0205 to 0.0277—approximately 40 to 50% greater than those observed in the Patient 1 dataset. Both the mean and maximum sNND errors for the Patient 2 dataset decrease from $0.75\,T$ to $1.0\,T$, as we fit sequentially from the closed to open valve configurations. The Patient 2 dataset required weight parameter adjustments as discussed above due to higher noise levels. The reduced relative importance of the Chamfer distance loss term compared

to the regularization terms is the primary contributor to the increase in sNND error.

Table 5: Patient 2 dataset: Minimum, maximum and mean sNND errors between the fitted B-spline surface and target point clouds at different stages of the cardiac cycle.

Step	Minimum sNND	Maximum sNND	Mean sNND
$0.75\,T$	4.14×10^{-5}	0.1359	0.0277
$0.80\,T$	4.59×10^{-6}	0.1273	0.0230
$0.85\,T$	6.41×10^{-6}	0.1241	0.0229
$0.93\,T$	1.40×10^{-5}	0.0924	0.0212
$1.0\,T$	3.86×10^{-4}	0.0931	0.0205

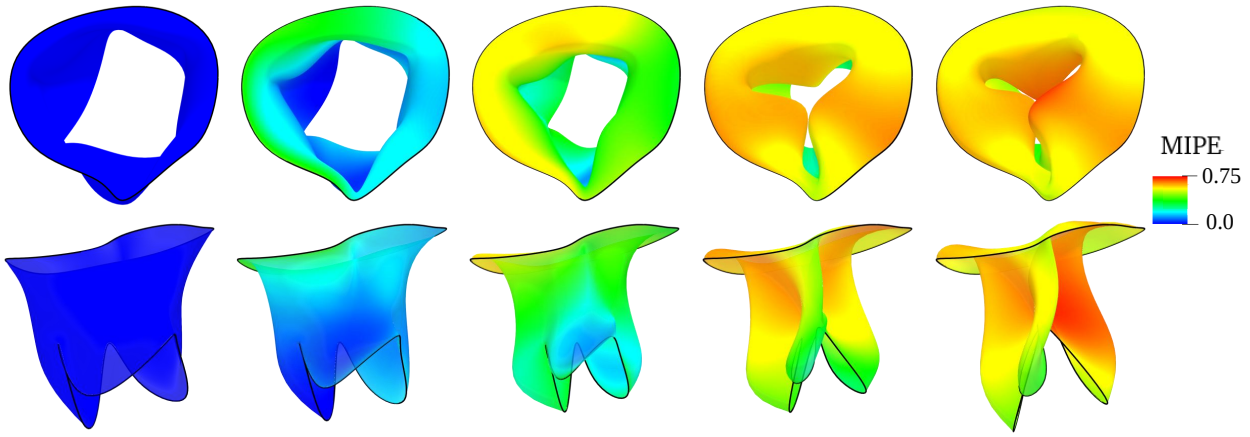
The loss function in Eq. 2 does not contain any explicitly defined regularization terms to prevent global intersections, which may occur when fitting highly noisy or irregular point clouds. Intersections are avoided by employing the one-sided chamfer distance (Eq. 5) from the point cloud to the B-spline surface. Using the one-sided Chamfer distance prevents the issue of multiple surface points converging toward the same point in the point cloud when fitting extremely sparse point cloud data. Through hyperparameter tuning, the VALVEFIT framework balances geometric regularity and fitting accuracy when dealing with different noise levels. Thus, this framework can be used for generating analysis-suitable patient-specific B-spline surfaces for a variety of patient datasets with varying image quality and segmentation accuracy.

4.5. Tricuspid Valve Structural Simulation

Accurate modeling of TV closure under systolic loads is vital for predicting regurgitation and supporting surgical planning. To demonstrate the utility of our framework in patient-specific applications, we perform a simplified simulation on the fitted B-spline surface and highlight its ability to extract meaningful metrics such as strain. In this study, we adopt the isogeometric analysis framework developed by Johnson et al. [20] to simulate valve closure using a patient-specific surface fitted with VALVEFIT framework.

For this simulation, the point cloud for Patient 2 at $1.0\,T$ is considered to be the initial, stress-free configuration. The leaflet material behavior is modeled using the isotropic Lee–Sacks model [78], where the strain energy functional is defined as $\frac{1}{2}c_0(I_1-3)+\frac{1}{2}c_1(e^{c_2(I_1-3)^2}-1)$. Here, I_1 is the first invariant (trace) of the left Cauchy–Green deformation tensor, and c_0, c_1, and c_2 are the material coefficients set to c_0 = 10 kPa, c_1 = 0.209 kPa, and c_2 = 9.046 [79]. The leaflet's mass density is set at 1.0 g/cm^3 with a thickness of 0.0396 cm.

Accurate TV dynamics requires modeling the chordae tendineae, as healthy chordae play an important role in preventing valve prolapse. Without them, the valve cannot properly seal, leading to regurgitation and other functional impairments. Despite their importance to valve function, it is



(a) t = 0.0 s **(b)** t = 0.0064 s **(c)** t = 0.0120 s **(d)** t = 0.0240 s **(e)** Steady state

Figure 16: A series of snapshots illustrating the closing behavior of the tricuspid valve from top and side views. The color indicates the maximum in-plane principal Green–Lagrange strain (MIPE) on the atrial side of the leaflets. A pressure load of 25 mmHg increases linearly over the course of 5 milliseconds, mirroring the physiological pressure gradient across the TV during systole for this simulation.

difficult for current non-invasive imaging techniques to capture chordae with enough fidelity for accurate geometric modeling. Previous efforts have worked around this issue by creating functional chordae maps [80] or using interactive dynamic simulations to estimate chordae location heuristically to match patient-valve behavior [81].

This work uses simplified chordae to prevent leaflet prolapse and demonstrate how the geometry is directly analysis suitable through closure mechanics. Six idealized cables, each 1 cm in length, are attached to the leaflet and extend outwards perpendicular to its surface. Each TV leaflet has two chordae, with one end of each chordae attached to an insertion point along the free edge of the TV and the other fixed in space to represent papillary muscle attachment. An IGA cable formulation [20] is used for the chordae, which are modeled as cubic B-spline curves with Young's modulus of 40 MPa and a fictitious radius of 0.023 cm. This setup ensures that the valve is constrained and resists leaflet prolapse. For more accurate patient-specific simulations, proper insertion points and papillary muscle locations can be used for more clinically viable results.

The simulations specifically focus on the tricuspid valve in its closed state. For simplification, the positions of the annulus and papillary muscles are fixed in the initial configuration of $1.0\,T$, and thus their motion or deformation is not modeled. Valve closure is achieved by applying a pressure load on the ventricular side of the leaflet surface. This load increases linearly from 0 to 25 mmHg over the course of 5 milliseconds (0 to 0.005 s), mirroring the physiological pressure gradients across the TV during systole.

Figure 16 shows the top and side views of the simulated valve closure, highlighting the framework's ability to produce patient-specific, analysis-suitable geometries for predictive modeling. These geometries allow for the recovery of valuable cardiac cycle metrics, including deformation, coaptation, and strain (e.g. MIPE, the maximum in-plane principal Green–Lagrange strain), which are often inaccessible through clinical imaging alone. With access to more complete patient data, it should be possible to recover physiologically relevant, patient-specific metrics throughout the entire cardiac cycle.

5. Conclusion

In this article, we introduce VALVEFIT, a novel GPU-accelerated B-spline surface fitting framework for 3D surface reconstruction of tricuspid heart valve geometry from noisy and sparse point cloud data obtained via medical image segmentation. In this approach, surface fitting is carried out by deforming a template B-spline geometry. We introduce novel regularization terms that maintain the local orthogonality of the surface tangent vectors and constrain the variation of the normal vectors to ensure that the underlying B-spline surface is smooth and intersection-free. The resulting B-spline surfaces are suitable for biomechanical simulations. We first validated the VALVEFIT framework with a benchmark point cloud dataset that is derived from structural simulation. Here, we also demonstrate robustness toward fitting varying point cloud density and increasing noise intensity. Finally, we have demonstrated surface fitting for real patient data, where we accurately captured the complex three-leaflet structure of the tricuspid valve. The fitted surfaces closely approximate the inherent valve geometry represented by the point clouds across multiple time points in the cardiac cycle. We demonstrate that the fitted surfaces are suitable for biomechanical analysis by performing a structural simulation of the fitted geometry and obtaining strain distribution during valve deformation. These patient-specific valve geometries can offer insight into the progression of valve-related complications, enabling biomechanical modeling-guided precise and effective interventions.

Despite these successes, there are some limitations and scope for improvements for VALVEFIT. While we were able to generate non-intersecting surfaces without any explicit terms in the loss function to model contact, certain patient-specific scenarios may still lead to leaflet intersections. In our future work, we plan to incorporate an explicit contact term in the loss function to prevent intersections. This will also allow us to fit the closing stages of heart valves more accurately. We also plan to extend the VALVEFIT framework to support volumetric spline parameterization and patient-specific volumetric modeling for isogeometric analysis.

Code Availability

The code is available at https://github.com/CMIA-Lab/ValveFit.git under the MIT license.

Acknowledgments

A. Moola and A. Pawar would like to acknowledge funding from the Translational AI Center at Iowa State University. A.M. Corpuz and M.-C. Hsu would like to acknowledge funding from the National Science Foundation under award number DMS-2436623. C.-H. Lee would like to acknowledge support from the National Institutes of Health (R01HL159475, R01GM157589), the American Heart Association (16SDG27760143, 24IVPHA1283213), and the Oklahoma Center for the Advancement of Science and Technology (OCAST HR23-03). This support is gratefully acknowledged.

References

[1] D. Lloyd-Jones, R. J. Adams, T. M. Brown, M. Carnethon, S. Dai, G. De Simone, T. B. Ferguson, E. Ford, and K. Furie. Heart disease and stroke statistics–2010 update: A report from the American Heart Association. *Circulation*, 121(7):e46–e215, 2010.

[2] R. B. Hinton and K. E. Yutzey. Heart valve structure and function in development and disease. *Annual Review of Physiology*, 73(1):29–46, 2011.

[3] Centers for Disease Control and Prevention (CDC). Heart valve disease, 2024. URL https://www.cdc.gov/heart-disease/about/heart-valve-disease.html.

[4] K. A. Jayakumar, L. J. Addonizio, M. R. Kichuk-Chrisant, M. E. Galantowicz, J. M. Lamour, J. M. Quaegebeur, and D. T. Hsu. Cardiac transplantation after the Fontan or Glenn procedure. *Journal of the American College of Cardiology*, 44(10):2065–2072, 2004.

[5] R. G. Ohye, D. Schranz, and Y. D'Udekem. Current therapy for hypoplastic left heart syndrome and related single ventricle lesions. *Circulation*, 134(17):1265–1279, 2016.

[6] R. Gobergs, E. Salputra, and I. Lubaua. Hypoplastic left heart syndrome: A review. *Acta Medica Lituanica*, 23(2):86, 2016.

[7] V. Rai, M. Gładki, M. Dudyńska, and J. Skalski. Hypoplastic left heart syndrome [HLHS]: Treatment options in present era. *Indian Journal of Thoracic and Cardiovascular Surgery*, 35:196–202, 2019.

[8] P. M. McCarthy, S. K. Bhudia, J. Rajeswaran, K. J. Hoercher, B. W. Lytle, D. M. Cosgrove, and E. H. Blackstone. Tricuspid valve repair: Durability and risk factors for failure. *The Journal of Thoracic and Cardiovascular Surgery*, 127(3):674–685, 2004.

[9] C.-H. Lee, D. W. Laurence, C. J. Ross, K. E. Kramer, A. R. Babu, E. L. Johnson, M.-C. Hsu, A. Aggarwal, A. Mir, H. M. Burkhart, R. A. Towner, R. Baumwart, and Y. Wu. Mechanics of the tricuspid valve—from clinical diagnosis/treatment, in-vivo and in-vitro investigations, to patient-specific biomechanical modeling. *Bioengineering*, 6:47, 2019.

[10] M. Enriquez-Sarano, D. Messika-Zeitoun, Y. Topilsky, C. Tribouilloy, G. Benfari, and H. Michelena. Tricuspid regurgitation is a public health crisis. *Progress in Cardiovascular Diseases*, 62(6):447–451, 2019.

[11] F. Condello, M. Gitto, and G. G. Stefanini. Etiology, epidemiology, pathophysiology and management of tricuspid regurgitation: An overview. *Reviews in Cardiovascular Medicine*, 22(4):1115–1142, 2021.

[12] C. J. Ross, A. Mir, H. M. Burkhart, G. A. Holzapfel, and C.-H. Lee. Tricuspid valve regurgitation in hypoplastic left heart syndrome: Current insights and future perspectives. *Journal of Cardiovascular Development and Disease*, 10:111, 2023.

[13] W. Sun, C. Martin, and T. Pham. Computational modeling of cardiac valve function and intervention. *Annual Review of Biomedical Engineering*, 16(1):53–76, 2014.

[14] P. Lancellotti, C. Tribouilloy, A. Hagendorff, B. A. Popescu, T. Edvardsen, L. A. Pierard, L. Badano, and J. L. Zamorano. Recommendations for the echocardiographic assessment of native valvular regurgitation: An executive summary from the European Association of Cardiovascular Imaging. *European Heart Journal–Cardiovascular Imaging*, 14(7):611–644, 2013.

[15] L. P. Badano, E. Agricola, L. P. de Isla, P. Gianfagna, and J. L. Zamorano. Evaluation of the tricuspid valve morphology and function by transthoracic real-time three-dimensional echocardiography. *European Journal of Echocardiography*, 10(4):477–484, 2009.

[16] D. Muraru, R. T. Hahn, O. I. Soliman, F. F. Faletra, C. Basso, and L. P. Badano. 3-dimensional echocardiography in imaging the tricuspid valve. *JACC: Cardiovascular Imaging*, 12(3): 500–515, 2019.

[17] G. Yan, Y. Liu, M. Xie, J. Shi, W. Qiao, and N. Dong. Experimental and computational models for tissue-engineered heart valves: A narrative review. *Biomaterials Translational*, 2 (4):361, 2021.

[18] Y. J. Zhang. *Geometric Modeling and Mesh Generation from Scanned Images*. Chapman and Hall/CRC, 2016.

[19] M. S. Sacks, A. Khalighi, S. Rego, B.and Ayoub, and A. Drach. On the need for multi-scale geometric modelling of the mitral heart valve. *Healthcare Technology Letters*, 4(5): 150, 2017.

[20] E. L. Johnson, D. W. Laurence, F. Xu, C. E. Crisp, A. Mir, H. M. Burkhart, C.-H. Lee, and M.-C. Hsu. Parameterization, geometric modeling, and isogeometric analysis of tricuspid valves. *Computer Methods in Applied Mechanics and Engineering*, 384:113960, 2021.

[21] M. S. Sacks, F. J. Schoen, and J. E. Mayer Jr. Bioengineering challenges for heart valve tissue engineering. *Annual Review of Biomedical Engineering*, 11(1):289–313, 2009.

[22] M. S. Sacks, W. D. Merryman, and D. E. Schmidt. On the biomechanics of heart valve function. *Journal of Biomechanics*, 42(12):1804–1824, 2009.

[23] M. Toma, C. H. Bloodworth IV, D. R. Einstein, E. L. Pierce, R. P. Cochran, A. P. Yoganathan, and K. S. Kunzelman. High-resolution subject-specific mitral valve imaging and modeling: experimental and computational methods. *Biomechanics and Modeling in Mechanobiology*, 15(6):1619–1630, 2016.

[24] G. Gaidulis, K.S. Suresh, D. Xu, and M. Padala. Patient-specific three-dimensional ultrasound derived computational modeling of the mitral valve. *Annals of Biomedical Engineering*, 50(7):847–859, 2022.

[25] R. Haj-Ali, G. Marom, S. B. Zekry, M. Rosenfeld, and E. Raanani. A general three-dimensional parametric geometry of the native aortic valve and root for biomechanical modeling. *Journal of Biomechanics*, 45(14):2392–2397, 2012.

[26] R. Miller, E. Kerfoot, C. Mauger, T. F. Ismail, A. A. Young, and D. A. Nordsletten. An implementation of patient-specific biventricular mechanics simulations with a deep learning and computational pipeline. *Frontiers in Physiology*, 12:716597, 2021.

[27] M. Toma, S. Singh-Gryzbon, E. Frankini, Z. Wei, and A. P. Yoganathan. Clinical impact of computational heart valve models. *Materials*, 15(9):3302, 2022.

[28] A. M. Pouch, H. Wang, M. Takabe, B. M. Jackson, J. H. Gorman, R. C. Gorman, P. A. Yushkevich, and C. M. Sehgal. Fully automatic segmentation of the mitral leaflets in 3D transesophageal echocardiographic images using multi-atlas joint label fusion and deformable medial modeling. *Medical Image Analysis*, 18:118–129, 2014.

[29] O. K. Ginty, J. T. Moore, M. Eskandari, P. Carnahan, A. Lasso, M. A. Jolley, M. Monaghan, and T. M. Peters. Dynamic, patient-specific mitral valve modelling for planning transcatheter repairs. *International Journal of Computer Assisted Radiology and Surgery*, 14:1227–1235, 2019.

[30] M. Mathur, W. D. Meador, M. Malinowski, T. Jazwiec, T. A. Timek, and M. K. Rausch. Texas trivalve 1.0: A reverse-engineered, open model of the human tricuspid valve. *Engineering with Computers*, 38(5):3835–3848, 2022.

[31] E. Votta, E. Caiani, F. Veronesi, M. Soncini, F. M. Montevecchi, and A. Redaelli. Mitral valve finite-element modelling from ultrasound data: a pilot study for a new approach to understand mitral function and clinical scenarios. *Philosophical Transactions of the Royal Society A: Mathematical, Physical and Engineering Sciences*, 366(1879):3411–3434, 2008.

[32] M. Stevanella, E. Votta, M. Lemma, C. Antona, and A. Redaelli. Finite element modelling of the tricuspid valve: A preliminary study. *Medical Engineering & Physics*, 32(10):1213–1223, 2010.

[33] F. Zhang, J. Kanik, T. Mansi, I. Voigt, P. Sharma, R. I. Ionasec, L. Subrahmanyan, B. A. Lin, L. Sugeng, and D. Yuh. Towards patient-specific modeling of mitral valve repair: 3D transesophageal echocardiography-derived parameter estimation. *Medical Image Analysis*, 35:599–609, 2017.

[34] N. T. Simonian, H. Liu, S. Vakamudi, M. J. Pirwitz, A. M. Pouch, J. H. Gorman III, R. C. Gorman, and M. S. Sacks. Patient-specific quantitative in-vivo assessment of human mitral valve leaflet strain before and after mitraclip repair. *Cardiovascular Engineering and Technology*, 14(5):677–693, 2023.

[35] H. Liu, N. T. Simonian, A. M. Pouch, P. A. Iaizzo, J. H. Gorman, R. C. Gorman, and M. S. Sacks. A computational pipeline for patient-specific prediction of the postoperative mitral valve functional state. *Journal of Biomechanical Engineering*, 145(11), 2023.

[36] R. Munafò, S. Saitta, G. Ingallina, P. Denti, F. Maisano, E. Agricola, A. Redaelli, and E. Votta. A deep learning-based fully automated pipeline for regurgitant mitral valve anatomy analysis from 3D echocardiography. *IEEE Access*, 2024.

[37] F. Xu, S. Morganti, R. Zakerzadeh, D. Kamensky, F. Auricchio, A. Reali, T. J. R. Hughes, M. S. Sacks, and M.-C. Hsu. A framework for designing patient-specific bioprosthetic heart valves using immersogeometric fluid-structure interaction analysis. *International Journal for Numerical Methods in Biomedical Engineering*, 34:e2938, 2018.

[38] M. Abbasi and A. N. Azadani. A geometry optimization framework for transcatheter heart valve leaflet design. *Journal of the Mechanical Behavior of Biomedical Materials*, 102: 103491, 2020.

[39] X. G. Pan, A. M. Corpuz, M. R. Rajanna, and E. L. Johnson. Parameterization, algorithmic modeling, and fluid–structure interaction analysis for generative design of transcatheter aortic valves. *Engineering with Computers*, 40:3405–3427, 2024.

[40] T. J. R. Hughes, J. A. Cottrell, and Y. Bazilevs. Isogeometric analysis: CAD, finite elements, NURBS, exact geometry, and mesh refinement. *Computer Methods in Applied Mechanics and Engineering*, 194:4135–4195, 2005.

[41] A. Li, X. Chai, G. Yang, and Y. J. Zhang. An isogeometric analysis computational platform for material transport simulation in complex neurite networks. *Molecular & Cellular Biomechanics*, 16(2):123–140, 2019.

[42] X. Wei, Y. J. Zhang, T. J. R. Hughes, and M. A. Scott. Truncated hierarchical Catmull–Clark subdivision with local refinement. *Computer Methods in Applied Mechanics and Engineering*, 291:1–20, 2015.

[43] X. Wei, Y. J. Zhang, T. J. R. Hughes, and M. A. Scott. Extended truncated hierarchical Catmull–Clark subdivision. *Computer Methods in Applied Mechanics and Engineering*, 299: 316–336, 2016.

[44] X. Wei, Y. J. Zhang, and T. J. R. Hughes. Truncated hierarchical tricubic C^0 spline construction on unstructured hexahedral meshes for isogeometric analysis applications. *Computers & Mathematics with Applications*, 74(9):2203–2220, 2017.

[45] X. Wei, Y. Zhang, L. Liu, and T. J. R. Hughes. Truncated T-splines: Fundamentals and methods. *Computer Methods in Applied Mechanics and Engineering*, 316:349–372, 2017.

[46] X. Wei, Y. J. Zhang, D. Toshniwal, H. Speleers, X. Li, C. Manni, J. A. Evans, and T. J. R. Hughes. Blended b-spline construction on unstructured quadrilateral and hexahedral meshes with optimal convergence rates in isogeometric analysis. *Computer Methods in Applied Mechanics and Engineering*, 341:609–639, 2018.

[47] H. Casquero, X. Wei, D. Toshniwal, A. Li, T. J. R. Hughes, J. Kiendl, and Y. J. Zhang. Seamless integration of design and Kirchhoff–Love shell analysis using analysis-suitable unstructured T-splines. *Computer Methods in Applied Mechanics and Engineering*, 360:112765, 2020.

[48] S. Morganti, F. Auricchio, D. J. Benson, F. I. Gambarin, S. Hartmann, T. J. R. Hughes, and A. Reali. Patient-specific isogeometric structural analysis of aortic valve closure. *Computer Methods in Applied Mechanics and Engineering*, 284:508–520, 2015.

[49] W. Zhang, G. Rossini, D. Kamensky, T. Bui-Thanh, and M. S. Sacks. Isogeometric finite element-based simulation of the aortic heart valve: Integration of neural network structural material model and structural tensor fiber architecture representations. *International Journal for Numerical Methods in Biomedical Engineering*, 37:e3438, 2021.

[50] W. Zhang, S. Motiwale, M.-C. Hsu, and M. S. Sacks. Simulating the time evolving geometry, mechanical properties, and fibrous structure of bioprosthetic heart valve leaflets under cyclic loading. *Journal of the Mechanical Behavior of Biomedical Materials*, 123:104745, 2021.

[51] X. Feng, Y. Liu, D. Kamensky, D. W. McComb, C. K. Breuer, and M. S. Sacks. Functional mechanical behavior of the murine pulmonary heart valve. *Scientific Reports*, 13:12852, 2023.

[52] K. Takizawa, T. E. Tezduyar, T. Terahara, and T. Sasaki. Heart valve flow computation with the integrated Space–Time VMS, Slip Interface, Topology Change and Isogeometric Discretization methods. *Computers & Fluids*, 158:176–188, 2017.

[53] T. Terahara, K. Takizawa, T. E. Tezduyar, Y. Bazilevs, and M.-C. Hsu. Heart valve isogeometric sequentially-coupled FSI analysis with the space–time topology change method. *Computational Mechanics*, 65:1167–1187, 2020.

[54] T. Terahara, T. Kuraishi, K. Takizawa, and T. E. Tezduyar. Computational flow analysis with boundary layer and contact representation: II. Heart valve flow with leaflet contact. *Journal of Mechanics*, 38:185–194, 2022.

[55] M. C. H. Wu, H. M. Muchowski, E. L. Johnson, M. R. Rajanna, and M.-C. Hsu. Immersogeometric fluid–structure interaction modeling and simulation of transcatheter aortic valve replacement. *Computer Methods in Applied Mechanics and Engineering*, 357:112556, 2019.

[56] E. L. Johnson, M. C. H. Wu, F. Xu, N. M. Wiese, M. R. Rajanna, A. J. Herrema, B. Ganapathysubramanian, T. J. R. Hughes, M. S. Sacks, and M.-C. Hsu. Thinner biological tissues induce leaflet flutter in aortic heart valve replacements. *Proceedings of the National Academy of Sciences*, 117:19007–19016, 2020.

[57] F. Xu, E. L. Johnson, C. Wang, A. Jafari, C.-H. Yang, M. S. Sacks, A. Krishnamurthy, and M.-C. Hsu. Computational investigation of left ventricular hemodynamics following bio-

prosthetic aortic and mitral valve replacement. *Mechanics Research Communications*, 112: 103604, 2021.

[58] E. L. Johnson, M. R. Rajanna, C.-H. Yang, and M.-C. Hsu. Effects of membrane and flexural stiffnesses on aortic valve dynamics: Identifying the mechanics of leaflet flutter in thinner biological tissues. *Forces in Mechanics*, 6:100053, 2022.

[59] A. Balu, S. Nallagonda, F. Xu, A. Krishnamurthy, M.-C. Hsu, and S. Sarkar. A deep learning framework for design and analysis of surgical bioprosthetic heart valves. *Scientific Reports*, 9(1):18560, 2019.

[60] M. S. Sacks, S. Motiwale, C. Goodbrake, and W. Zhang. Neural network approaches for soft biological tissue and organ simulations. *Journal of Biomechanical Engineering*, 144:121010, 2022.

[61] K. Meyer, C. Goodbrake, and M. S. Sacks. A neural network finite element trileaflet heart valve model incorporating multi-body contact. *International Journal for Numerical Methods in Biomedical Engineering*, 41:e70038, 2025.

[62] A. Aggarwal, V. S. Aguilar, C.-H. Lee, G. Ferrari, J. H. Gorman, R. C. Gorman, and M. S. Sacks. Patient-specific modeling of heart valves: From image to simulation. In S. Ourselin, D. Rueckert, and N. Smith, editors, *Functional Imaging and Modeling of the Heart*, pages 141–149, Berlin, Heidelberg, 2013. Springer.

[63] A. Aggarwal, A. M. Pouch, E. Lai, J. Lesicko, P. A. Yushkevich, J. H. Gorman III, R. C. Gorman, and M. S. Sacks. In-vivo heterogeneous functional and residual strains in human aortic valve leaflets. *Journal of Biomechanics*, 49:2481–2490, 2016.

[64] A. D. Prasad, A. Balu, H. Shah, S. Sarkar, C. Hegde, and A. Krishnamurthy. NURBS-Diff: A differentiable programming module for NURBS. *Computer-Aided Design*, 146:103199, 2022.

[65] A. Moola, A. Balu, A. Krishnamurthy, and A. Pawar. THB-Diff: A GPU-accelerated differentiable programming framework for THB-splines. *Engineering with Computers*, pages 1–17, 2023.

[66] D. P. Gramling, A. L. van Veldhuisen, F. W. Damen, K. Thatcher, F. Liu, D. McComb, J. Lincoln, C. K. Breuer, C. J. Goergen, and M. S. Sacks. In vivo three-dimensional geometric reconstruction of the mouse aortic heart valve. *Annals of Biomedical Engineering*, 52:2596–2609, 2024.

[67] M. H. Park, Y. Zhu, A. M. Imbrie-Moore, H. Wang, M. Marin-Cuartas, M. J. Paulsen, and Y. J. Woo. Heart valve biomechanics: the frontiers of modeling modalities and the expansive capabilities of ex vivo heart simulation. *Frontiers in Cardiovascular Medicine*, 8:673689, 2021.

[68] K. Mah, N. S. Khoo, E. Tham, M. Yaskina, M. Maruyama, B. J. Martin, S. Alvarez, N. Alami, I. M. Rebeyka, J. Smallhorn, and T. Colen. Tricuspid regurgitation in hypoplastic left heart syndrome: Three-dimensional echocardiography provides additional information in describing jet location. *Journal of the American Society of Echocardiography*, 34(5):529–536, 2021. doi: 10.1016/j.echo.2020.12.010.

[69] Slicer Community. 3D slicer: A platform for medical image informatics, image processing, and three-dimensional visualization, 2024. URL http://www.slicer.org.

[70] A. Fedorov, R. Beichel, J. Kalpathy-Cramer, J. Finet, J. Fillion-Robin, S. Pujol, C. Bauer, D. Jennings, F. Fennessy, and M. Sonka. 3D Slicer as an image computing platform for the Quantitative Imaging Network. *Magnetic Resonance Imaging*, 30(9):1323–1341, 2012.

[71] L. Piegl and W. Tiller. *The NURBS Book (Monographs in Visual Communication), 2nd ed.* Springer-Verlag, New York, 1997.

[72] X. Li and M. A. Scott. Analysis-suitable T-splines: Characterization, refineability, and approximation. *Mathematical Models and Methods in Applied Sciences*, 24(06):1141–1164, 2014.

[73] X. Wei, X. Li, K. Qian, T.J.R. Hughes, Y. J. Zhang, and H. Casquero. Analysis-suitable unstructured T-splines: Multiple extraordinary points per face. *Computer Methods in Applied Mechanics and Engineering*, 391:114494, 2022.

[74] J. Bradbury, R. Frostig, P. Hawkins, M. J. Johnson, C. Leary, D. Maclaurin, G. Necula, A. Paszke, J. VanderPlas, S. Wanderman-Milne, and Q. Zhang. JAX: composable transformations of Python+NumPy programs, 2018. URL http://github.com/jax-ml/jax.

[75] D. P. Kingma and J. Ba. ADAM: A method for stochastic optimization, 2017. URL https://arxiv.org/abs/1412.6980.

[76] F. van der Heijden. *Image based measurement systems: object recognition and parameter estimation*. Wiley, United States, November 1994. ISBN 978-0-471-95062-2.

[77] A. V. Nguyen, A. Lasso, H. H. Nam, J. Faerber, A. H. Aly, A. M. Pouch, A. B. Scanlan, F. X. McGowan, L. Mercer-Rosa, M. S. Cohen, J. Simpson, G. Fichtinger, and M. A. Jolley.

Dynamic three-dimensional geometry of the tricuspid valve annulus in hypoplastic left heart syndrome with a fontan circulation. *Journal of the American Society of Echocardiography*, 32(5):655–666, 2019.

[78] M. C. H. Wu, R. Zakerzadeh, D. Kamensky, J. Kiendl, M. S. Sacks, and M.-C. Hsu. An anisotropic constitutive model for immersogeometric fluid–structure interaction analysis of bioprosthetic heart valves. *Journal of Biomechanics*, 74:23–31, 2018.

[79] D. Kamensky, F. Xu, C.-H. Lee, J. Yan, Y. Bazilevs, and M.-C. Hsu. A contact formulation based on a volumetric potential: Application to isogeometric simulations of atrioventricular valves. *Computer Methods in Applied Mechanics and Engineering*, 330:522–546, 2018.

[80] H. Narang, A. H. Khalighi, R. C. Gorman, and M. S. Sacks. Noninvasive patient–specific simulations of mitral valve surgical repair using a high-fidelity functionally equivalent chordae representation. *Structural Heart*, 5(5):56–68, 2021. doi: 10.1080/24748706.2021.1901502.

[81] L. Walczak, L. Tautz, M. Neugebauer, et al. Interactive editing of virtual chordae tendineae for the simulation of the mitral valve in a decision support system. *International Journal of Computer Assisted Radiology and Surgery*, 16:125–132, 2021. doi: 10.1007/s11548-020-02230-y.